An epigenome atlas of neural progenitors within the embryonic mouse forebrain

Christopher T. Rhodes[1], Joyce J. Thompson[2], Apratim Mitra[3], Dhanya Asokumar[1,2], Dongjin R. Lee[1], Daniel J. Lee[1,2], Yajun Zhang[1], Eva Jason[3], Ryan K. Dale[3], Pedro P. Rocha[2,4], Timothy J. Petros[1]

[1]Unit on Cellular and Molecular Neurodevelopment

[2]Unit on Genome Structure and Regulation

[3]Bioinformatics and Scientific Programming Core

Eunice Kennedy Shriver National Institute of Child Health and Human Development (NICHD), National Institutes of Health (NIH), Bethesda, MD 20892, USA.

[4]National Cancer Institute (NCI), NIH, Bethesda, MD 20982, USA.

***Correspondence: tim.petros@nih.gov**

Keywords: Interneuron, Neurodevelopment, Epigenetic, Chromatin Accessibility, Single cell sequencing

ABSTRACT

A comprehensive characterization of epigemonic organization in the embryonic mouse forebrain will enhance our understanding of neurodevelopment and provide insight into mechanisms of neurological disease. We collected single-cell chromatin accessibility profiles from four distinct neurogenic regions of the embryonic mouse forebrain using single nuclei ATAC-Seq (snATAC-Seq). We identified thousands of differentially accessible peaks, many restricted to distinct progenitor cell types or brain regions. We integrated snATAC-Seq and single cell transcriptome data to characterize changes of chromatin accessibility at enhancers and promoters with associated transcript abundance. Multi-modal integration of histone modifications (CUT&Tag and CUT&RUN), promoter-enhancer interactions (Capture-C) and high-order chromatin structure (Hi-C) extended these initial observations. This dataset reveals a diverse chromatin landscape with region-specific regulatory mechanisms and genomic interactions in distinct neurogenic regions of the embryonic mouse brain and represents an extensive public resource of a ‘ground truth’ epigenomic landscape at this critical stage of neurogenesis.

INTRODUCTION

Inhibitory GABAergic interneurons are a heterogeneous cell population that can be classified based on electrophysiological properties, morphologies, synaptic connectivity, neurochemical markers and transcriptomes[1-3]. In the forebrain, GABAergic neurons are born from transient embryonic structures in the ventral telencephalon known as the medial, caudal and lateral ganglionic eminences (MGE, CGE, and LGE, respectively), whereas glutamatergic projection neurons arise from the dorsal telencephalon. The MGE and CGE (and adjacent preoptic area) generate nearly all cortical and hippocampal interneurons, with each region generating almost entirely distinct, non-overlapping interneuron subtypes[4-6].

The embryonic brain contains two primary classes of neural progenitors: multipotent self-renewing apical progenitors (APs, also known as radial glia cells) located in the ventricular zone (VZ) and basal progenitors (BPs) that undergo neurogenic divisions within the subventricular zone (SVZ)[7]. Both APs and BPs give rise to postmitotic immature neurons (Ns) within the GEs that migrate tangentially to populate the telencephalon. Recent evidence demonstrates that initial interneuron subtype fate is specified within the GEs as interneuron progenitors exit the cell cycle[8-11]. It is well established that changes in a cell's epigenetic landscape alters cell fate decisions throughout normal development[12,13] and can be associated with neurodevelopmental disorders[14-16]. In fact, many neurological and psychiatric disease-associated genes are expressed during embryonic development[17,18] and are enriched specifically in APs and immature interneurons[19,20]. Furthermore, many neurological disorders have been linked directly to polymorphisms in enhancer regions[21,22], and GWAS indicate that >90% of disease-associated single nucleotide polymorphisms (SNPs) are located outside of coding regions[23]. Thus, a thorough characterization of the epigenomic landscape during neurogenesis is necessary to understand normal development and potential disease etiologies.

Using a single nuclei assay for transposase accessible chromatin followed by sequencing (snATAC-Seq)[24], we characterized the chromatin accessibility of cells during the transition from

51 progenitors to lineage restricted neurons within the GEs and dorsal telencephalon of the
52 embryonic mouse brain. We identified differentially accessible peaks (DA peaks) enriched in
53 specific brain regions and/or distinct progenitor cell types. Among chromatin accessibility profiles,
54 individual loci smoothly transition from open to closed chromatin (or vice versa) during the initial
55 stages of neurogenesis. We validated our snATAC-Seq and single cell RNA sequencing (scRNA-
56 Seq) observations with orthogonal epigenomic methods. Genome-wide histone modification
57 profiles associated with promoters (H3K4me3), active enhancers (H3K27ac) and gene repression
58 (H3K27me3) were highly concordant with our snATAC-Seq profiles showing spatially restricted
59 enrichment patterns. Our single-cell derived gene-enhancer models largely agreed with direct
60 observations of promoter-enhancer interactions by Capture-C and higher-order chromatin
61 domains by Hi-C. These data are available as a UCSC Genome Browser track hub, providing an
62 important new resource for the field to explore spatial differences in the chromatin landscape of
63 distinct neuronal progenitors within the embryonic mouse forebrain.
64

65 **RESULTS**

66 **Identifying chromatin accessibility profiles in the embryonic forebrain**

67 To ascertain the chromatin accessibility landscape of differentiating neurons, we dissected
68 the MGE, CGE, LGE and cortex from wild-type mice at embryonic day 12.5 (E12.5) when cells in
69 the GEs are undergoing neurogenesis[4] and processed single nuclei on the 10X Genomics
70 platform (Fig. 1a). Since cortical neurogenesis occurs later, we also harvested E14.5 dorsal cortex
71 to compare both temporally (E12.5 GEs vs. E12.5 cortex) and neurogenically (E12.5 GEs vs.
72 E14.5 cortex) matched dorsal and ventral forebrain. Sequencing libraries contained 39,253 single
73 nuclei, with 10,310 from MGE, 8,543 from CGE, 11,346 from LGE and 9,054 from cortex. Libraries
74 were aggregated, downsampled to equal numbers of median fragments per nuclei and normalized
75 by latent semantic analysis (LSA) before peak calling, construction of cell-by-peak count matrices
76 and integration of different samples (Extended Data Fig. 1a-g).

77 Using uniform manifold approximation and projection (UMAP), nuclei segregated largely
78 by tissue region (Fig. 1b). The smart local moving (SLM) algorithm[25] detected 27 clusters, of which
79 three non-neuronal clusters were removed to retain 96.8% of nuclei in 24 clusters (Fig. 1c). Cell
80 types were assigned by inspecting promoter accessibility (PA) (defined as the sum of reads
81 mapping within -2000 bp of a TSS) of canonical cell type markers and were further refined by
82 transferring cell type assignments from droplet-based scRNA-Seq data of E12.5 embryos (Fig.
83 1d and Extended Data Fig. 1i-n) to the snATAC-seq dataset. PA for markers of interneuron and
84 excitatory glutamatergic pyramidal cell maturation segregated clusters into mitotic APs and BPs,
85 and postmitotic Ns (Fig. 1D and Extended Data Fig. 1o-q). MGE and most CGE and LGE nuclei
86 displayed accessible chromatin at GABAergic neuron markers, while virtually all cortical nuclei
87 have accessible chromatin at markers of glutamatergic neurons (Extended Data Fig. 1o and
88 Extended Data Fig. 2). A group of LGE and CGE nuclei displayed accessibility profiles more
89 similar to glutamatergic neuron markers and were labeled as a 'mixed' neuron population
90 (Extended Data Fig. 1o and Extended Data Fig. 2). This was likely contamination from the pallial-
91 subpallial boundary (PSB), a region that gives rise to cells located in the piriform cortex, claustrum
92 and amygdala[26,27].
93 To quantify temporal differentiation programs, a minimum spanning tree was constructed
94 in Monocle3[28,29] (Fig. 1e). The progression along pseudotime largely recapitulated known
95 maturation markers, from *Nes*+ and *Ccnd2*+ cycling progenitors to *Dcx*+ and *Rbfox3*+ postmitotic
96 neurons (Fig. 1f-i). Additionally, region restricted genes such as *Nkx2-1* and *Lhx6* in the MGE,
97 and *Neurod6* in the cortex, displayed open accessibility profiles restricted to these regions (Fig.
98 1j-m). We examined pseudobulk ATAC read pileups within each cluster for regionally restricted
99 genes for the MGE (*Nkx2-1*) and cortex (*Neurod6*) (Fig. 1n-o) and for two pan-neuronal
100 maturation markers for APs (*Nes*) and BPs/Ns (*Dcx*) (Fig. 1p-q). High signal strength for *Nkx2-1*
101 and *Neurod6* reads were restricted to the MGE and cortex/mixed clusters, respectively. As
102 expected, *Nes* reads were enriched in AP clusters with diminished signals in BP and N clusters,

103 whereas *Dcx* displayed the inverse low-AP to high-N accessibility profile. Notably, strong
104 accessibility was detected in the second intron of *Nes* which contains a known enhancer[30] (Fig.
105 1p). These observations were in agreement with ENCODE H3K4me3 ChIP-Seq data from E12.5
106 mouse forebrain (Fig. 1n-q).
107
108 **Differentially accessible peak profiles during neurogenesis**
109 When comparing differentially accessible (DA) peaks among all possible peaks (intergenic
110 peaks and those in promoters/gene bodies), we sought to detect cluster and cell type specific
111 markers, detecting a total of 30,046 DA peaks (FDR <= 0.05, average log(fold change) > 0) across
112 all clusters (Fig. 2a, Extended Data Fig. 3a, and Supplementary Table 1). These DA peaks
113 represent accessible genomic loci that are potentially unique to specific cell types. To characterize
114 DA peak profiles across clusters, we asked whether the genomic coordinates bounding DA peaks
115 of one cluster had reads in any other cluster. If there were reads in a DA peak from one cluster in
116 another cluster, this peak was considered overlapping between the clusters. No minimum
117 threshold for overlapping peak counts was used before calculating the percentage of overlapping
118 DA peaks from one cluster compared to all peaks from the same cluster (Fig. 2a, "% Overlap").
119 We also counted the number of DA peaks from each cluster to assess if there were differences
120 in the number of DA peaks per cluster (Fig. 2a, "Peak counts").
121 Unsupervised hierarchical clustering (HC) of DA peak profiles created a dendrogram that
122 segregated clusters initially by maturation state (AP, BP and N) and secondarily by tissue origin.
123 Since the overall profiles of LGE and CGE nuclei were very similar, these two regions were
124 labeled 'LGE/CGE' for this analysis. The 'mixed' neuron population (Extended Data Fig. 1o) was
125 also left as an individual group for this analysis. The dendrogram generated by HC is very similar
126 to cluster relationships in LSA/UMAP space, which is encouraging since different features were
127 used in each analysis (HC: DA peaks in cluster pairs, LSA: all peaks across libraries). As
128 expected, dot plot positions containing both high DA peaks counts and high percent overlap were

129 almost exclusively grouped along the diagonal, while positions with limited numbers of DA peaks
130 or low between-cluster peak overlap populated the off-diagonals, indicating high specificity of DA
131 peaks to specific clusters (Fig. 2a). The cell type- and brain region-specific DA peak profiles are
132 consistent with previous models of chromatin reorganization during cellular differentiation[31,32].

133 We also visualized binarized peak signals (i.e., “open” or “closed” regions) per cluster
134 using a heatmap and again observed high peak signals primarily along the diagonal (Extended
135 Data Fig. 3a). Intriguingly, the mean number of DA peaks decreased as maturation progressed,
136 with a significant decrease in DA peaks in BP and N nuclei compared to APs in each tissue
137 (Extended Data Fig. 3c-d). Despite this decrease, DA peak profiles became more distinct as
138 maturation progressed, as indicated by the low between-cluster peak overlap along the dot plot
139 off-diagonals (Fig. 2a and Extended Data Fig. 3a). The decrease in global accessibility over time
140 is consistent with previous observations during cellular differentiation[33]. We observed a greater
141 number of DA peaks in all maturation stages in the cortex compared to GEs (Extended Data Fig.
142 3e-f).

143 Regions of accessible chromatin are enriched for transcription factor (TF) binding motifs
144 that often play essential roles in driving cell specification. To characterize region-enriched TF
145 motifs, we performed motif analysis on DNA sequences within DA peaks using the JASPAR
146 CORE[34] vertebrates collection. Motif analysis detected TF motifs that have lineage- and tissue-
147 specific roles during interneuron neurogenesis (Fig. 2a, Extended Data Fig. 3b and
148 Supplementary Table 2). Further, among motifs enriched in specific clusters that also had a
149 corresponding differentially accessible promoter, the top 5 matches contain one or more TF motifs
150 with known spatial or temporal expression profiles correlating with the cell cluster (Fig. 2b and
151 Supplementary Table 3). For example, UMAP visualization of motif enrichment by chromVAR[35]
152 for NR2F1 (MGE and CGE-specific)[36], ASCL1 (GABAergic BP-enriched), EMX1 (cortical
153 progenitor AP/BP-specific) and NEUROD2 (cortical postmitotic N-specific) motifs demonstrated
154 the expected neuronal lineage progression and/or region-restricted patterns (Fig. 2b-e). We

155 further quantified genome-wide DA peak distributions within annotated gene regions and found
156 the majority of DA peaks were constrained to promoter and intronic regions of gene bodies, and
157 distal intergenic loci (Extended Data Fig. 3g). These findings indicate that DA peaks are specific
158 to brain region and cell-state, and importantly, that DA peaks contain lineage-specific TF motifs
159 that may regulate cell fate decisions differentiation.
160

161 **Candidate cis-regulatory elements are dynamic and cell state dependent**

162 The global decrease of DA peak numbers from cycling neural progenitors to postmitotic
163 immature neurons prompted us to examine changes to DA peaks during maturation and lineage
164 commitment. For this and all future analysis, we removed the 'mixed' population to characterize
165 only LGE and CGE-derived GABAergic cells. The Monocle3 extension Cicero[37] detects
166 interactions or 'connections' between any 2 genomic loci and then assigns a co-accessibility score
167 between the 2 sites, thereby calculating the proportion of nuclei containing a given co-accessibility
168 interaction within a population. We quantified such interactions within all nuclei and detected
169 92,414 connections that had a co-accessibility score equal to or greater than 0.25, meaning a
170 given locus-locus interaction is detectable in $\geq$ 25% of all nuclei in the defined population
171 (henceforth "Cicero connections").

172 To explore co-accessibility changes during neurogenesis, we used a heatmap to visualize
173 Cicero connections in which at least one of the 2 interacting loci was a DA peak, representing
174 potential interactions between DA peaks and putative cis-regulatory elements (cREs). Nuclei were
175 divided into 10 bins of equal pseudotime intervals along the Y-axis, with individual DA peaks
176 grouped via hierarchical clustering along the X-axis. The heatmap color represents the proportion
177 of nuclei with a given DA peak (interacting via a Cicero connection) with a co-accessibility score
178 $\geq$ 0.25 (Fig. 3a). Nearly half of these Cicero connections were enriched in AP nuclei, which is
179 consistent with an overall decrease in accessibility as development progresses (Extended Data
180 Fig. 3c-d). As chromatin regions with dynamic accessibility are associated with gene regulation

181 during neural stem cell activation[32], we hypothesized that Cicero connections enriched in
182 immature neurons encode lineage-specific cREs that may play a role in neuronal lineage
183 commitment.

184 To identify candidate cREs at specific genes, we examined Cicero connections within 0.5
185 Mb windows of gene TSSs after filtering for co-accessibility scores $\geq$ 0.25. We identified Cicero
186 connections in which only one of the 2 interacting loci overlapped a TSS, representing potential
187 interactions between a TSS and putative cREs (henceforth "TSS-cRE connections"). All Cicero
188 connections within this 0.5 Mb window are visualized as orange arcs whereas TSS-cRE
189 connections for a selected gene are highlighted in purple (Fig. 3b-c). To characterize Cicero
190 connections that were spatially restricted, we downsampled tissues to equal nuclei numbers and
191 detected 91,904, 76,858, 89,366, and 148,942 Cicero connections with co-accessibility scores $\geq$
192 0.25 in MGE, LGE, CGE and cortex, respectively. *Lhx6* and *Neurod6* Cicero connections are
193 restricted to the MGE and cortex, respectively, and TSS-cRE connections for *Lhx6* and *Neurod6*
194 are virtually exclusive to these regions (Fig. 3b). *Nr2f2* (*CoupTF-II*) is a marker for APs in the VZ
195 of the CGE and caudal MGE[38] whereas *Sp8* is a marker for LGE progenitors that is excluded from
196 the MGE[39]; both genes displayed highest co-accessibility scores and TSS-cRE connections
197 counts in the expected regions (Fig. 3b). Overall, tissue specific TSS-cRE connectivity patterns
198 were similar to regionally restricted gene expression patterns that are critical to neuronal
199 development.

200 To characterize Cicero connections that varied between neurogenic cell types, we
201 downsampled to equal nuclei numbers and detected 89,312, 88,980, and 110,362 Cicero
202 connections with co-accessibility scores $\geq$ 0.25 in AP, BP and N nuclei, respectively. Among these
203 Cicero connections, postmitotic genes *Lhx6* and *Neurod6* had their highest co-accessibility scores
204 and TSS-cRE connections in BP and N nuclei (Fig. 3c). Progenitor-enriched genes *Nr2f2* and *Sp8*
205 had their highest co-accessibility scores and TSS-cRE connections in APs, with decreased
206 connections and co-accessibility scores in Ns. The pan-AP marker nestin (*Nes*) had its highest

207 co-accessibility scores and TSS-cRE connections in APs throughout all regions compared to BPs
208 and Ns. Conversely, the postmitotic GABAergic marker *Gad1* had its highest co-accessibility
209 scores and connection counts in BPs and Ns. As with regional specificity of TSS-cRE
210 connections, the temporal connection patterns largely recapitulate known gene expression
211 patterns as neurons mature. In sum, cREs likely interact with DA peaks and TSSs to regulate
212 genes in regionally and temporally restricted patterns, and the co-accessibility patterns of TSS-
213 cREs connections closely resemble known spatial and temporal expression patterns in the
214 embryonic forebrain.
215
216 **Integrative analysis of chromatin accessibility and gene expression profiles**
217 To enhance our understanding of the relationship between chromatin accessibility and
218 gene expression during neurogenesis, we combined chromatin accessibility profiles from
219 snATAC-Seq data with age and region-matched scRNA-Seq data. Integrating ATAC and RNA
220 data involves quantifying ATAC reads in or near gene bodies by a Gene Activity Score (GAS) as
221 a proxy for transcript abundance. After testing multiple GAS metrics for snATAC-Seq/scRNA-Seq
222 integration, we defined GAS as the sum of all ATAC reads mapping to the promoter, first exon
223 and presumptive enhancers of a given gene because this GAS metric produced the highest
224 concordance between ATAC and RNA assays (Extended Data Fig. 4). Following integration, the
225 clustering of snATAC-Seq and scRNA-Seq cells were highly concordant, with the MGE and cortex
226 integrated cells formed distinct clusters whereas the LGE and CGE cells were largely overlapping
227 (Fig. 4a-b). The Louvain algorithm detected 26 clusters (Fig. 4c) and Monocle3 assigned
228 pseudotime (Fig. 4d) which largely recapitulated temporal and spatially restricted expression
229 patterns expected in embryonic forebrain neurogenic regions (Fig. 4e-j and Extended Data Fig.
230 5).
231 Prior to integration, we refined our cRE predictions to detect presumptive enhancers by
232 combining our Cicero TSS-cRE analysis with TSS-cRE predictions from the SnapATAC

233 algorithm[40] (Supplementary Table 4). SnapATAC predictions link distal regulatory elements to
234 target genes based on the transcript count of a gene and chromatin accessibility at peaks flanking
235 the gene using gene expression as input variable to predict the binarized chromatin state at peaks.
236 Our rationale for using multiple algorithms was TSS-cREs connections common to both methods
237 likely improves cRE predictions. After combining TSS-cRE connections from both methods, we
238 retained common cREs to generate a list of all detectable presumptive enhancers (Extended Data
239 Fig. 6). We took the intersection of these loci and ENCODE H3K27ac ChIP-Seq peaks[41] from
240 E12.5 and E14.5 forebrain, resulting in a set of 'high-confidence' enhancer candidates (henceforth
241 "presumptive enhancers") (Supplementary Table 5). We detected previously validated VISTA
242 enhancers[42] interacting with genes in the MGE (hs704 and hs1538 regulating *Nkx2-1*), cortex
243 (hs627 regulating *Neurod2*), GABAergic progenitors (hs967, hs998, hs1114, hs1354, and hs1540
244 regulating *Ascl1*) and glutamatergic progenitors (hs1025 regulating *Emx1*) (Fig. 4k-n and
245 Supplementary Table 6).

246 To characterize the temporal expression and chromatin accessibility profiles during
247 neurogenesis, we utilized a hierarchical clustering based approach from the DEGReport package[43]
248 to group RNA, GAS and enhancer counts from our integrated scRNA-Seq/snATAC-Seq data (Fig. 5a-
249 r). As not all genes had detectable snATAC based GAS and/or enhancer counts, we selected ~300
250 of the most differentially expressed genes (DEGs) (from scRNA) among APs, BPs and Ns that
251 had corresponding GAS and enhancer counts. DEGReports hierarchical clustering uncovered 5
252 groups containing at least 6 genes (Extended Data Fig. 7a-b), of which over 85% of the genes fell
253 into two categories: one cluster is consistent with high expression and accessibility profiles within
254 progenitors (APs and BPs) that are downregulated in postmitotic neurons (156 DEGs, Fig. 5a),
255 and another cluster with the complimentary profile (90 DEGs, Fig. 5b). Genes within these clusters
256 displayed similar patterns of expression and chromatin accessibility over pseudotime.
257 Visualization of representative early-expressed genes *Hes1* (Fig. 5c-f) and *Lmo1* (Fig. 5g-j) and
258 later-expressed genes *Myt1l* (Fig. 5k-n) and *Lhx6* (Fig. 5o-r) demonstrate consistent trends for

259 transcript, GAS and enhancer counts over pseudotime. We quantified the number of high-
260 confidence enhancers associated with upregulated DEGs as maturation progressed and
261 identified 200 enhancers associated with DEGs that had a positive fold change from APs-to-BPs,
262 175 enhancers for BPs-to-Ns, and 269 enhancers from APs-to-Ns (Extended Data Fig. 7c).
263 Likewise, we found 188 enhancers associated with DEGs that had a negative fold change from
264 APs-to-BPs, 179 enhancers for BPs-to-Ns, and 320 enhancers from APs-to-Ns (Extended Data
265 Fig. 7c). There is a gradual decrease in the ratio of the number of enhancers being activated
266 versus the number being decommissioned as maturation progressed (Extended Data Fig. 7d),
267 suggesting that a greater number of genes and associated enhancers are repressed as
268 progenitors exit the cell cycle. Taken together, DEGs and associated enhancers exhibit
269 reorganization during the transition from progenitors to lineage committed postmitotic immature
270 neurons.

271 We characterized the differentiation processes by visualizing matched heatmaps for RNA,
272 GAS and presumptive enhancer counts of highly variable genes (Fig. 5s-u). We selected
273 transcript counts and corresponding GAS and enhancer counts for the top 500 most variable
274 genes from the E12.5 integrated dataset, of which 210 had corresponding GAS and enhancer
275 counts (Extended Data Fig. S7e-g). RNA, GAS and enhancer count matrices for these genes
276 were co-clustered using hierarchical clustering with a correlation distance metric and average
277 linkage and visualized in matched heatmaps (Fig. 5s-u). Partitioning early, transitional and late
278 expressing gene profiles with respect to pseudotime largely followed a continuous progression as
279 cells matured from APs through Ns. Overall, there was high similarity between 1) early and late
280 gene expression patterns detected by degPatterns (Fig. 5a-b and Extended Data Fig. 7a-b) and
281 2) early and late expressing genes visualized in heatmaps (Fig. 5s-u), indicating distinct, dynamic
282 expression and chromatin accessibility in APs, BPs and Ns. By integrating multiple single cell
283 modalities, we characterized the chromatin accessibility and gene expression profile of distinct
284 forebrain regions during neurogenesis.

285

286 **Histone modifications and higher-order chromatin organization reveal region-specifc**
287 **chromatin states**

288 Predicting enhancers from snATAC data has enormous potential for mapping regulatory
289 elements in heterogeneous cell populations. To validate some of these predictions, we carried
290 out two additional sets of experiments. First, we preformed CUT&RUN[44] and CUT&Tag[45] on E12.5
291 MGE, LGE, CGE and cortex to detect histone modifications associated with active/poised
292 promoters (H3K4me3), active enhancers (H3K27ac) and repressed genes (H3K27me3)[46-48]. Most
293 genes with spatially-restricted mRNA and promoter accessibility profiles contained corresponding
294 H3K4me3 peaks whereas spatially-repressed genes were enriched with H3K27me3 (Fig. 6a).
295 More globally, we observed ~70% of ATAC peaks at promoters overlapped with H3K4me3 marks
296 in all brain regions (Fig. 6b).

297 To further identify candidate enhancers, we combined our Cicero analysis with H3K27ac
298 enrichment. There was less overlap between ATAC peaks and H3K27ac marks (29.2%-45.1%),
299 as expected due to the weaker correlation between accessibility and H3K27ac marks throughout
300 the genome. However, if we restricted analysis to ATAC peaks with a Cicero connection to a
301 promoter (indicative of possible enhancers), then the percent overlap of ATAC peaks with
302 H3K27ac marks increased considerably (54.9%-68.1%) (Fig. 6b).

303 We observed region-specific colocalization between ATAC peaks, Cicero connections and
304 H3K27ac marks at many genes, some of which represent novel candidate enhancers. For
305 example, there are VISTA enhancers downstream of the GE-enriched *Ascl1*, with one site
306 (hs1540) showing co-accessibilty in nearly all nuclei (Fig. 6c). However, none of these VISTA
307 reporters displayed the expected GE-restricted *Ascl1* expression pattern
308 (https://enhancer.lbl.gov) nor contained GE-enriched H3K27ac marks (Fig. 6c). Instead, we
309 identified two other regions with Cicero interactions with GE-enriched H3K27ac marks compared
310 to cortex (Fig. 6c, grey bars). We identified similar loci near *Lhx6* and *Neurog2* with enriched

311 H3K27ac marks specifically in the MGE and cortex, respectively, representing potentially novel
312 cREs (Fig. 6d-e).

313 We performed Hi-C to characterize chromatin structure genome wide (Fig. 7a) and
314 Capture-C to directly quantify promoter interactions at ~50 genes with tissue-specific expression
315 patterns (Fig. 7b and Supplementary Table 7). At the *Nkx2-1* locus, Hi-C data revealed formation
316 of an MGE-specific chromatin domain compared to other brain regions (Fig. 7a). Capture-C
317 confirmed these distinct interactions, with the *Nkx2-1* promoter interacting directly with a region
318 near the *Mbip* gene specifically in the MGE (Fig. 7b). Notably, *Mbip* expression is also restricted
319 to the MGE during development[49]. Conversely, interactions between the *Nkx2-1* promoter and the
320 *Nkx2-9* and *Pax9* loci (genes not expressed in the embryonic forebrain) were specifically detected
321 in the LGE, CGE and cortex (Fig. 7b). While the exact nature of these interactions is unclear
322 (promoter-enhancer, promoter-promoter, etc.), the formation of region-specific chromatin
323 domains is not observable from the other assays, as the snATAC and histone modifications at
324 the *Mbip*, *Nkx2-9* and *Pax9* locus are quite similar between the different brain regions (Fig. 7c).

325 Both Hi-C and Capture-C data identified a direct interaction between the *Nr2f1* promoter
326 and an intron within *2210408I21Rik* specific to the CGE and MGE, where *Nr2f1* is expressed[36]
327 (Fig. 7d-e). This locus also contains stronger K27ac signal in the CGE and MGE (Fig. 7f),
328 providing additional evidence for formation of region-specific promoter-enhancer interactions.
329 Similarly, we observe cortex-enriched interactions of the *Lhx2* promoter with two putative
330 enhancers within *Dennd1a* introns, with both loci displaying stronger H3K27ac signals in the
331 cortex compared to other regions (Fig. 7g-i).

332 Thus, the combination of single cell accessibility and transcriptomes, histone modifications
333 and higher-order chromatin interactions represents a comprehensive epigenomic 'ground truth'
334 of distinct neurogenic regions of the embryonic mouse brain that give rise to specific neuronal
335 subtypes. These data are publicly available and searchable as a UCSC Genome Browser track
336 hub (See Data Availability section).

337

338 **DISCUSSION**

339 We characterized the single cell chromatin accessibility and transcriptomic profiles, histone
340 modifications and higher order chromatin organization in four distinct neurogenic regions of the
341 mouse embryonic forebrain. While recent studies performed single cell sequencing experiments
342 to characterize chromatin accessibility in the mouse and human forebrain[31,50-52], our dataset
343 represents the most comprehensive analysis of the chromatin landscape in the developing brain
344 to date. With this combinatorial approach, we characterized the variation and dynamic
345 reconfiguration of mRNA, gene accessibility and active enhancers during neurogenesis and
346 across different neurogenic cell types. We identified numerous candidate enhancers for genes
347 involved in well-characterized neuronal subtypes, many with region-specific direct genomic
348 interactions verified by Hi-C and Capture-C. These data are publicly available in an easily
349 searchable platform on the UCSC genome browser (See Data Availability section;
350 https://genome.ucsc.edu/cgi-bin/hgTracks?hubUrl=https://hpc.nih.gov/~BSPC-
351 Petros/track_hub/chromatin_quantification.hub.txt&hgS_loadUrlName=https://hpc.nih.gov/~BSP
352 C-Petros/track_hub/session.txt&hgS_doLoadUrl=submit). This dataset will be an important
353 resource for the field leading to a greater understanding of the genetic and epigenetic
354 mechanisms regulating initial neuronal fate decision in the embryonic forebrain.

355 Gene expression and DA peaks were strongly correlated with H3K4me3 and H3K27me3
356 peaks at active and repressed promoters, respectively, in specific brain regions. There was also
357 a high correlation between ATAC peaks with Cicero connections to gene promoters and H3K27ac
358 marks at these ATAC peaks (Fig. 6b), indicative of likely active enhancers. In most instances,
359 there was a lag for chromatin at genes and enhancers to become inaccessible compared to RNA
360 downregulation, both at the individual gene level (Fig. 5c-r) and global level (Fig. 5s-u). This
361 observation implies that some repressive mechanisms (i.e. repressor TFs, DNA methylation, etc.)
362 likely precede repressive histone modifications and decreased chromatin accessibility at cREs.

363 We observed numerous instances where accessibility of promoters, gene body and/or enhancers
364 precede transcript upregulation (e.g., *Nkx2-1* in Fig. 4g-h and *Myt1l* and *Lhx6* in Fig. 5k-r), which
365 is in agreement with several recent reports[51,53]. Future multiomics studies that can simultaneously
366 capture the epigenome and transcriptome within single cells during development should provide
367 significant insight into this relationship.

368 By performing Hi-C and Capture-C on dissected MGE, LGE, CGE and cortex, we
369 characterized region-specific chromatin domains and enhancer-promoter interactions *in vivo* that
370 were not previously identifiable in ENCODE or other studies that do not distinguish between
371 different forebrain regions. For example, the *Nkx2-1* chromatin domain is markedly different
372 between the MGE (where *Nkx2-1* directly contacts the *Mbip* locus) and non-MGE (where *Nkx2-1*
373 directly contacts the *Nkx2-9* and *Pax9* locus) (Fig. 7). Perturbing these types of interactions could
374 reveal important insights into how chromatin organization affects promoter-enhancer interactions
375 and gene function in a region-specific manner. As we only examined ~50 genes with Capture-C,
376 the realm of region-specific interactions between genes and cREs in the developing forebrain is
377 only beginning to be explored. Previous comparative analyses of chromatin structure have
378 described organ and cell type-specific spatial configurations, but have focused mostly on adult
379 tissues[54,55]. Analysis of cell populations representing earlier stages of differentiation trajectories
380 have been mostly restricted to the immune system[56,57], limb differentiation[58] and other
381 organisms[59,60] and have revealed lower variation of chromatin structure between different cell
382 types. In contrast, our data show that spatially adjacent cells representing early neuronal
383 specification processes can present vastly heterogenous 3D chromatin strcutures.

384 We note several additional intriguing observations from our data. First, the chromatin
385 accessibility profiles reveal significant diversity in AP clusters from the GEs, much more so than
386 cortical APs which have greater similarity between each other compared to other clusters (Fig.
387 2). Much of the reported transcriptional diversity within the GEs has been restricted to postmitotic

388 cells[8,9], so our data suggests that there may be greater transcriptional and chromatin state
389 diversity in GE APs than previously appreciated[61].

390 Second, the number and score of global Cicero connections near a particular gene
391 (orange arcs from Fig. 3b-c) are only loosely correlated to TSS-cRE connections. In some
392 instances, the number of global Cicero connections at certain genomic loci appear to be tissue
393 specific (greater co-accessibility in regions flanking *Neurod6* restricted to cortex and *Lhx6*
394 restricted to MGE), while global Cicero connections near other genes appear more similar
395 between tissues (similar co-accessibility for all brain regions flanking *Sp8* and *Nr2f2*). This may
396 suggest a role of Cis-Co-accessibility Networks (CCANs)[37], modules of connection sites that are
397 highly co-accessible with one another in specific brain regions during neuronal fate determination.

398 Third, the population of 'mixed' cells that were collected with the LGE and CGE tissue
399 expressed markers for both GABAergic and glutamatergic cells yet formed a distinct cluster from
400 the cortex and GE populations (Fig. 2 and Extended Data Fig. 2). These 'mixed' cells likely reside
401 at the PSB as they were not detected in the MGE population. The diversity of cells arising from
402 the lateral/ventral pallium remains poorly characterized, but this region appears to give rise to
403 glutamatergic cells of the insular cortex, piriform cortex, claustrum and pallial amygdala[26]. A recent
404 scRNAseq study may shed light on the heterogeneity of this PSB region[27], but further work is
405 needed to better characterize this cell population.

406 In sum, the single cell chromatin accessibility and transcript profiles, histone modifications,
407 and higher-order chromatin structure define the epigenetic "ground truth" of distinct forebrain
408 regions during initial neuronal fate decisions. This resource will aid our understanding of normal
409 development and neurological disease as many disease-associated genes are enriched in neural
410 progenitors and immature neurons[19,20], and many disease-associated SNPs are located in non-
411 coding enhancer regions[21-23].

412

413 **ACKNOWLEDGEMENTS**

We thank S. Henikoff for pA-Tn5 transposome; S. Coon, J. Iben, T. Li and other members of the NICHD Molecular Genomic Core; C. J. McBain, K. Pelkey, J. A. Kassis and members of the Petros Lab for helpful discussions. Further information and requests for resources and reagents should be directed to and will be fulfilled by the Lead Contact, Timothy J. Petros (tim.petros@nih.gov).

AUTHOR CONTRIBUTIONS

C.T.R and T.J.P. designed the study and wrote the paper. C.T.R., Y.Z. and T.J.P. extracted and purified nuclei. D.R.L. and T.J.P. extracted and purified embryonic cells. Y.Z. prepared single cell sequencing libraries. C.T.R., A.M., D.R.L. and R.K.D. analyzed single cell data. D.J.L., D.A., J.J.T., C.T.R. and P.P.R. performed and analyzed CUT&Tag and CUT&RUN experiments. J.J.T. and P.P.R. performed and analyzed Hi-C and Capture-C experiments. E.J. prepared the UCSC browser page. P.P.R., R.K.D. and T.J.P. supervised the project.

COMPETING INTERESTS STATEMENT

The authors declare no competing interests.

440 **METHODS**

441 **Animals.** The following mouse lines were used in this study: C57BL/6J (JAX# 000664). For timed
442 matings, noon on the day a vaginal plug was observed was denoted E0.5. All experimental
443 procedures were conducted in accordance with the National Institutes of Health guidelines and
444 were approved by the NICHD Animal Care and Use Committee (ACUC). Both male and female
445 embryonic and adult mice were used without bias for the single cell sequencing reactions.

446

447 **Tissue dissection.** To recover embryonic tissue, dams were anesthetized with isoflurane and
448 then euthanized by cervical dislocation. Embryos were removed from the uterus and kept in
449 chilled artificial cerebrospinal fluid (ACSF, in mM: 87 NaCl, 26 $NaHCO_3$, 2.5 KCl, 1.25 NaH_2PO_4,
450 0.5 $CaCl_2$, 7 $MgCl_2$, 10 glucose, 75 sucrose, saturated with 95% O_2, 5% CO_2, pH 7.4). Brains
451 were extracted from E12.5 and E14.5 embryos, hemisected, microdissected to obtain the MGE,
452 LGE, CGE and somatosensory cortex, and kept in ACSF.

453

454 **Nuclei extraction for single nuclei ATAC-seq, CUT&Tag and CUT&RUN.** Nuclei isolation
455 followed the 10X Genomics ATAC nuclei isolation protocol with several modifications. All steps
456 were performed on ice. For each brain region, tissue was transferred to a Dounce homogenizer
457 containing 1mL ATAC lysis buffer (10 mM Tris-HCL, pH 7.4, 10 mM NaCl, 3 mM MgCl2, 0.1%
458 Tween-20, 0.1% IGEPAL, 2% BSA). Samples were dounced with 10 strokes pestle A and 10
459 strokes pestle B. Lysate was strained through a 40 µm filter pre-wetted with ATAC wash buffer
460 (10 mM Tris-HCL, pH 7.4, 10 mM NaCl, 3 mM MgCl2, 0.1% Tween-20, 2% BSA) and neutralized
461 with 2 mL wash buffer.

462 For snATAC-Seq, lysates were centrifuged 500 g for 5 min at 4°C, supernatant removed,
463 nuclei pellet washed once with 1 mL wash buffer, and centrifuged 500 g for 5 min. A diluted aliquot
464 of nuclei solution was mixed with Trypan Blue (1:1) and counted on a hemocytometer. For all

465 samples, we prepared 3,000 nuclei/μL samples for snATACseq reactions, with 5 μL (~15,000
466 nuclei) used for each snATAC reaction.

467 For CUT&Tag/CUT&RUN, tissue was homogenized as described above. Nuclei
468 suspensions were centrifuged 500 g for 5 min at 4°C, supernatant removed, and washed once
469 with 1 mL wash buffer, centrifuged 500 g for 5 min and washed a final time with 1 mL 1X CUT&Tag
470 wash buffer (from CUT&Tag IT Assay Kit, Active Motif, #53610) or 1 mL CUT&RUN 1X wash
471 buffer (1 mL HEPES pH 7.5, 1.5 m 5M NaCl, 12.5 uL 2M spermidine and 47.5 mL dH_2O with 1
472 Roche Complete Protease Inhibitor EDTA-Free tablet). A diluted aliquot of nuclei solution was
473 mixed with Trypan Blue (1:1) and counted on a hemocytometer. Equal numbers of MGE, CGE,
474 LGE and cortex nuclei were pooled and diluted to a final concentration of 1000 nuclei/μL in wash
475 buffer, with 100 μL (~100,000 nuclei) used for each CUT&Tag/CUT&RUN reaction.

476

477 **Cell dissociation for single cell RNA-Seq, Hi-C and Capture-C.** Embryonic tissue was
478 dissected as described above. To collect whole cells, embryonic MGE, LGE, CGE and cortex
479 tissue was incubated in 1 mg/mL Pronase (Roche #10165921001) in ACSF for 20 minutes at RT.
480 Pronase solution was removed and 2 ml of reconstitution solution (1% fetal bovine serum +
481 DNAse (1:10,000, Roche #47167280001)) in oxygenated ACSF was added. For Hi-C and
482 Capture-C preparations, DNAse was not included in the reconsititution solution. Cells were
483 triturated sequentially with fire-polished large, medium and small bore Pasteur pipettes to
484 mechanically dissociate tissue.

485 For scRNA-Seq, DRAQ5 (20 μM) and DAPI (1:10,000) was added to the single cell
486 suspension, which was passed through a pre-wet 30 μm filter and then processed on an SH800
487 cell sorter to purify the sample. DRAQ5+/DAPI- live cells were collected in low-bind 1.5 mL tubes
488 containing 100 μL ACSF. Cell solutions were centrifuged at 300 g for 5 min at 4 ^{o}C in a swinging
489 bucket centrifuge and then counted on a hemocytometer. 15,000 cells (or highest amount
490 recovered after sorting) was used for 10X Genomics scRNA-Seq experiments.

491

492 **snATAC library preparation and sequencing.** snATAC reaction was carried out following 10X
493 Genomics ATAC User Guide (revision C), libraries were prepared following 10X Genomics and
494 Illumina guidelines, and sequenced on an Illumina HiSeq2500. Sequencing metrics were as
495 follows: **CGE**: Replicate 1: Read pairs: 469,280,227; Estimated number of cells: 4,013; Median
496 fragments per cell: 13,003; Fraction of fragments in peaks: 73.3%, Fraction of transposition events
497 in peaks: 58.4%. Replicate 2: Read pairs: 115,917,541; Estimated number of cells: 4,530; Median
498 fragments per cell: 11,082; Fraction of fragments in peaks: 80.3%, Fraction of transposition events
499 in peaks: 72.1%. **MGE**: Replicate 1: Read pairs: 429,523,963; Estimated number of cells: 6,845;
500 Median fragments per cell: 12,807; Fraction of fragments in peaks: 72.0%, Fraction of
501 transposition events in peaks: 54.2%. Replicate 2: Read pairs: 107,989,853; Estimated number
502 of cells: 3,465; Median fragments per cell: 12,278; Fraction of fragments in peaks: 77.4%, Fraction
503 of transposition events in peaks: 67.3%. **LGE**: Replicate 1: Read pairs: 491,904,518; Estimated
504 number of cells: 6,577; Median fragments per cell: 13,426; Fraction of fragments in peaks: 67.7%,
505 Fraction of transposition events in peaks: 47.4%. Replicate 2: Read pairs: 115,545,951; Estimated
506 number of cells: 4,769; Median fragments per cell: 10,660; Fraction of fragments in peaks: 77.7%,
507 Fraction of transposition events in peaks: 65.8%. **Cortex (E12.5)**: Read pairs: 112,120,408;
508 Estimated number of cells: 4,946; Median fragments per cell: 11,257; Fraction of fragments in
509 peaks: 78.0%, Fraction of transposition events in peaks: 68.1%. **Cortex (E14.5)**: Read pairs:
510 433,510,039; Estimated number of cells: 4,108; Median fragments per cell: 16,810; Fraction of
511 fragments in peaks: 74.2%, Fraction of transposition events in peaks: 63.6%.

512

513 **scRNA library preparation and sequencing.** cDNA libraries were prepared using 10X
514 Genomics 3' RNA v3 chemistry. Library preparation was carried out following 10X Genomics RNA
515 User Guide (rev C) and sequenced following 10X Genomics and Illumina guidelines. Samples
516 were sequenced to the following depths: **CGE**: Reads: 154,348,231; Estimated number of cells:

517 4,522; Median reads per cell: 34,133; Median genes per cell: 2,805. **MGE**: Reads: 192,833,398;
518 Estimated number of cells: 6,331; Median reads per cell: 30,459; Median genes per cell: 2,877.
519 **LGE**: Reads: 180,580,907; Estimated number of cells: 6,843; Median reads per cell: 26,389;
520 Median genes per cell: 2,726. **Cortex (E12.5)**: Reads: 176,542,467; Estimated number of cells:
521 7,453; Median reads per cell: 23,687; Median genes per cell: 2,318.
522
523 **CUT&Tag library preparation and sequencing.** Embryonic tissue was homogenized as
524 described above before proceeding with CUT&Tag. For each CUT&Tag replicate, 100,000 nuclei
525 were resuspended in 1.5 mL 1X Wash Buffer and then processed with the Active Motif CUT&Tag
526 IT Assay Kit (#53610) following manufacturer's instructions. Primary antibodies used: H3K4me3
527 (Active Motif, 39159), H3K27ac (Abcam, ab4729), H3K27me3 (Cell Signaling, 9733T). Following
528 library amplification, DNA quantity was determined with a Thermo Qubit and library quality
529 characterized with an Agilent Tapestation. Libraries were balanced for DNA content and pooled
530 before performing a final SPRIselect bead 1x left size selection and paired-end sequenced (50 x
531 50 bp) on an Illumina NovaSeq. Samples were sequenced to a following depths per library: **CGE**:
532 H3K27me3 Replicate 1: 13,604,105; H3K27me3 Replicate 2: 47,136,470; H3K4me3 Replicate 1:
533 50,541,513; H3K4me3 Replicate 2: 25,035,394; **CTX**: H3K27me3 Replicate 1: 13,640,572;
534 H3K27me3 Replicate 2: 36,097,462; H3K4me3 Replicate 1: 18,35,546; H3K4me3 Replicate 2:
535 30,114,008; **LGE**: H3K27me3 Replicate 1: 13,539,124; H3K27me3 Replicate 2: 30,498,855;
536 H3K4me3 Replicate 1: 14,760,336; H3K4me3 Replicate 2: 17,211,681; **MGE**: H3K27me3
537 Replicate 1: 17,214,723; H3K27me3 Replicate 2: 16,336,430; H3K4me3 Replicate 1: 5,518,769;
538 H3K4me3 Replicate 2: 14,720,921.
539
540 **CUT&RUN library preparation and sequencing.** Embryonic tissue was homogenized as
541 described above. Single nuclei suspensions were centrifuged 500g for 5 min at 4°C, supernatant
542 removed, and washed with 1 mL 1X Wash Buffer (1 mL HEPES pH 7.5, 1.5 m 5M NaCl, 12.5 uL

543 2M spermidine and 47.5 mL dH_2O with 1 Roche Complete Protease Inhibitor EDTA-Free tablet).
544 For each CUT&RUN replicate, 100,000 nuclei were resuspended in 1.5 mL 1X Wash buffer.
545 BioMag® Plus Concanavalin A beads (Bangs Laboratories) were washed in in Binding Buffer
546 (20mM HEPES pH 7.5, 10mM KCl, 1mM CaCl2, 1mM MnCl2). Nuclei were resuspended in Wash
547 Buffer, mixed with a slurry of the Concavalin A coated magnetic beads, and rotated for 10 minutes
548 at room temperature. 10 µl of Concavalin A bead slurry was used per 100,000 cells. The beads
549 were resuspended in Wash Buffer containing 2 mM EDTA, 0.1% bovine serum albumin, 0.05%
550 Digitonin, and 1:50 dilution of primary antibody, which was then incubated on a nutating platform
551 for 2 hours at room temperature. The beads were then washed twice in Digitonin Buffer (20 mM
552 HEPES pH 7.5, 150 mM NaCl, 0.5 mM Spermidine, 1x Roche Complete Protease Inhibitor no
553 EDTA, 0.05% Digitonin and 0.1% bovine serum albumin). Then they were incubated with pA-MN
554 (600 µg/ml, 1:200, either home-made or a gift from S. Henikoff) in Digitonin Buffer for 1 hour at
555 4ºC. Following this incubation, beads were washed twice with Digitonin Buffer and finally
556 resuspended in 150 µl of Digitonin Buffer, and equilibrated to 0ºC before adding CaCl2 (2mM).
557 The beads were then incubated for 1 hour at 0ºC. After this hou,150 µl of 2X Stop Buffer (200 mM
558 NaCl, 20 mM EDTA, 4 mM EGTA, 50 µg/ml RNase A, 40 µg/ml glycogen), was added. Beads
559 were incubated for 30 minutes at 37ºC and then pelleted at 16,000g for 5 minutes at 4ºC.
560 Supernatant was transferred, mixed with 3 µL 10% SDS and 1.8U Proteinase K (NEB), and
561 incubated for 1 hour at 50ºC, shaking at 900 rpm. 300 µl of 25:24:1 Phenol/Chloroform/Isoamyl
562 Alcohol was added, solutions were vortexed, and transferred to Maxtrack phase-lock tubes
563 (Qiagen). The samples in the phase-lock tubes were centrifuged at 16,000g for 3 minutes at room
564 temperature. 300 µl of Chloroform was added, solutions were mixed by inversion, and centrifuged
565 at 16,000g for 3 minutes at room temperature. Aqueous layers were transferred to new tubes and
566 DNA isolated through Ethanol precipitation. These samples were resuspended in 10mM Tris-HCl
567 pH 8.0 (ThermoFisher). CUT&RUN libraries were prepared following the SMARTer ThruPlex
568 TAKARA Library Prep kit with small modifications. Double stranded DNA (10 µl), Template

569 Preparation D Buffer (2 µl), and Template Preparation D Enzyme (1 µl) were combined and added
570 to each sample. End Repair and A-tailing was performed in a Thermocycler with a heated lid
571 (22ºC, 25 min; 55ºC, 20 min). To each sample, library Synthesis D Buffer (1 µl) and Library
572 Synthesis D Enzyme (1 µl) and library synthesis was performed (22ºC, 40 min). Library
573 Amplification D Buffer (25 µl), Library Amplification D Enzyme (1 µl), Nuclease-free water (4 µl),
574 and a unique Illumina-compatible indexed primer (5 µl) were added. Library amplification was
575 performed using the following conditions: 72ºC for 3 min; 85ºC for 2 min; 98ºC for 2 min
576 (denaturation); 4 cycles of 98ºC for 20 s, 67ºC for 20 s, 72ºC for 10 s (addition of indexes); 14
577 cycles of 98ºC for 20 s, 72ºC for 10 s (library amplification). Post-PCR clean-up involved
578 SPRIselect bead 0.6X left/1x right double size selection then washed twice gently in 80% ethanol,
579 and eluted in 10-12 µl 10 mM Tris pH 8.0. 1:50 Dilutions of primary antibodies against the following
580 active and repressive histone modifications were used: H3K4me3 (Active Motif, 39159), H3K27ac
581 (Abcam, ab4729) and H3K27me3 (Cell Signaling, 9733T). Following library amplification, DNA
582 quantity was determined with a Thermo Qubit and library quality characterized with an Agilent
583 Tapestation. Libraries were balanced for DNA content and pooled before performing a final
584 SPRIselect bead 1x left size selection and paired-end sequenced (50 x 50 bp) on an Illumina
585 NovaSeq. **CGE**: H3k27ac Replicate 1: 39,950,806; H3k27ac Replicate 2: 68,704,235; **CTX**:
586 H3k27ac Replicate 1: 45,279,956; H3k27ac Replicate 2: 73,920,447; **LGE**: H3k27ac Replicate 1:
587 46,933,225; H3k27ac Replicate 2: 55,438,848; **MGE**: H3k27ac Replicate 1: 55,871,849; H3k27ac
588 Replicate 2: 77,034,587.
589
590 **Hi-C and Capture-C library preparation and sequencing.** HiC and Capture-C were performed
591 and analyzed as described previously[62]. Embryonic tissue dissected and cells were dissociated
592 as described above. After dissociation, 1 million cells per region were fixed with 1% formaldehyde
593 (Thermo: 28908) made in 1 ml HBSS media. Fixation was carried out at room temperature on a
594 nutator, for 10 mins, protected from light. To stop fixation, glycine was added at a final

595 concentration of 0.13 M and samples were incubated for 5 mins at room temperature followed by
596 15 mins on ice. Fixed cells were then washed once with ice-cold PBS. After spinning cells at
597 2500g 4°C for 5 mins, the pellet was flash frozen in liquid nitrogen and stored at -80°C. To perform
598 Hi-C and Capture-C, pellets were first thawed on ice and then incubated with 1 ml lysis buffer (10
599 mM Tris-HCL pH8, 10 mM NaCl, 0.2% Igepal CA-630, Roche Complete EDTA-free Sigma
600 #11836170001). After lysis, cells were dounced and washed with cold PBS. Nuclei extracted with
601 this method were then collected by centrifugation and subjected to DpnII digest in 50 µl 0.5% SDS
602 and incubated at 62°C for 10 minutes after which 150 µl of 1.5% Triton-X was added and cells
603 incubated for 15 minutes at 37°C while shaking at 900 rpm. 25 µl of 10X DpnII restriction buffer
604 (NEB) was then added, and cells were incubated for 15 minutes while shaking. After that, 200U
605 of DpnII (NEB R0543M) were added and incubated for 2 hours, then 200U more and incubated
606 overnight. Next morning 200U more were added and incubated for 3h (total 600U of DpnII). DpnII
607 was inactivated at 62°C for 20 minutes. For Hi-C, biotin fill-in was done by incubating cells with a
608 mixture of 4.5 µl dCTP dTTP and dGTP at 3.3 mM, 8 µl klenow polymerase (NEB M0210L) and
609 37.5 µl Biotin-14-dATP (Thermo 19524016) for 4h at RT while shaking at 900 rpm for 10 seconds
610 every 5 minutes. Ligation was done overnight at 16°C also rotating at 900 rpm for 10 seconds
611 every 5 minutes by adding 120 µl of 10X ligation buffer (NEB), 664 µl water, 100 µl 10% Triton-
612 X, 6 µl BSA 20mg/ml, and 2 µl T4 ligase (NEB cat #M0202M). For Capture-C, biotin fill-in step
613 was skipped and 50 µl more of water was added to the ligation mix. Crosslink removal was done
614 overnight with 50 µl of proteinase K in 300 µl of following buffer (10 mM Tris-HCl pH8.0, 0.5 M
615 NaCl, 1%SDS) while shaking at 1400 rpm at 65°C. Following Sodium Acetate and 100% Ethanol
616 -80°C precipitation, DNA was resuspended in 50 µl 10 mM Tris HCL for Hi-C or 130 µl for Capture-
617 C. Sonication for Hi-C was done using Covaris onetube-10 AFA strips using the following
618 parameters for a 300 bp fragment size (Duration: 10 secs, repeat for 12 times, total time 120 secs,
619 peak power-20W, duty factor 40%, CPB-50). Sonication for Capture-C was done using Covaris
620 AFA microtubes 130 with following settings for a fragment size of 200 bp fragments (Duration:

621 225 secs, peak power-75W, duty factor 25%, Cycles per Burst-1000). Sonications were
622 performed in a Covaris ME220 sonicator. Sonicated material was then size selected using SPRI
623 beads with the following ratios: 0.55X and 1X for Capture-C and 0.55X and 0.75X for Hi-C. Hi-C
624 material was then bound, washed and recovered to 150 µl Streptavidin C1 beads (Thermo 65002)
625 per sample following manufacturers recommendations. Bead-bound DNA was resuspended in 50
626 µl 10 mM Tris HCl. Library preparation was done using Kapa Hyper Prep KK8502 kit. 10 µl of
627 End-repair buffer and enzyme mix were added to resuspended beads and incubated for 30
628 minutes at RT and then 30 minutes at 65°C. 1 µl of 15 mM annealed-Illumina adaptors, containing
629 an universal p5 and an indexed p7 oligo, were then incubated with a mixture containing 40 µl of
630 ligase and ligation buffer at RT for 60 minutes. Libraries were then amplified using 4 reactions per
631 sample for a total of 200 µl and 10 cycles, as recommended by manufacturer. For Capture-C,
632 following sonication and size selection, 1 µg of template material was resuspended in 50 µl of 10
633 mM Tris and used for library prep with 10 µl of End-Repair reaction. 5 µl of 15 mM annealed -
634 Illumina adaptors were ligated to the Capture-C material. Using a total volume of 100 µl, library
635 was amplified by PCR using 6 cycles. For capture, 1 µg of Capture-C library per sample was
636 mixed with mouse COT1 DNA and universal as well as index-specific blocking oligos from
637 SeqCap EZ HE-oligo (Roche). 4.5 µl pool of biotinylated probes (xGen Lockdown Probe Pools
638 from IDT), with each probe at 0.4 fmol/µl targeting the promoters of our loci of interested were
639 added to this mixture and incubated for 3 days at 47°C. Following binding to Streptavidin C1
640 beads, material was washed as recommended by the SeqCap EZ Hybridization and Wash Kits.
641 Following washes material was amplified by PCR using Kapa polymerase and 14 cycles. Material
642 from different samples was then combined and 1 µg of pooled libraries was recaptured in a single
643 reaction and amplified with 8 cycles. Probes for Capture-C were designed using Capsequm
644 (capsequm.molbiol.ox.ac.uk/cgi-bin/CapSequm.cgi) by selecting regions adjacent to the gene
645 promoters of interest. The list of probes used can be found in Supplementary Table 7.
646

647 **scRNA-Seq Analysis.** *Cellranger*: The Cellranger (v3.0.0) pipeline was used to process single
648 cell/nuclei RNA-Seq libraries, all steps used default parameters unless otherwise noted.
649 Cellranger mkfastq converted BCL files generated from sequencing to demultiplexed FASTQ files.
650 Reads were aligned to 10X Genomics's pre-built mouse (GRCm38/mm10) reference genome
651 with Cellranger count. For single cell RNA-Seq libraries, 10X Genomics's pre-built mRNA model
652 of GRCm38/mm10 annotation (refdata-cellranger-mm10-3.0.0) was used to map reads to genes,
653 while single nuclei RNA-Seq libraries used a corresponding pre-mRNA model constructed per
654 10X Genomics guidelines. Aligned reads were de-duplicated, filtered for valid cell barcodes and
655 used to construct gene-by-barcode matrices.

656 *Seurat*: Filtered gene-by-barcode matrices were used as input to Seurat (v3.0.0,
657 https://satijalab.org/seurat/) in R (v.4.0.0, https://cran.r-project.org/). For each cell barcode,
658 summary statistics were calculated for the metadata columns n_Features, n_genes, and percent
659 reads mapping to mitochondrial genes (if present). Outliers within the metadata columns were
660 detected using Tukey's fence method for far-out outliers ([Q1 - k(Q3 - Q1), Q3 + k(Q3 - Q1)],
661 where k = 3) which is resistant to extreme values (https://datatest.readthedocs.io/en/stable/how-
662 to/outliers.html) and barcodes with any metadata column that contained outliers were removed.
663 The remaining barcodes were processed using the SCTransform workflow in Seurat.
664

665 **snATAC-Seq Analysis.** *Cellranger-atac*: The Cellranger-atac (v1.2.0) pipeline was used to
666 process single nuclei ATAC-Seq data, all steps used default parameters unless otherwise noted.
667 Cellranger-atac mkfastq converted BCL files generated from sequencing to demultiplexed FASTQ
668 files. Reads were aligned to 10X Genomics's pre-built mouse (GRCm38/mm10) reference
669 genome and genomic annotation (refdata-cellranger-atac-mm10-1.2.0) by Cellranger-atac count.
670 Libraries were aggregated and downsampled to equal numbers of median fragments per nuclei
671 by Cellranger-atac aggr. Aligned reads were de-duplicated, filtered for valid cell barcodes, and
672 constructed peak-by-barcode and TF-by-barcode matrices and fragments file.

673 *Signac*: Filtered peak-by-barcode matrix and fragments file were analyzed using Signac
674 (v1.0.0) (https://satijalab.org/signac/index.html), all steps used default parameters unless
675 otherwise noted. For each cell, summary statistics were calculated for the metadata columns
676 n_Features, n_genes, and percent reads mapping to mitochondrial genes (if present). Outliers
677 within the metadata columns were detected using Tukey's fence method for far-out outliers, as
678 previously described, and barcodes with any metadata column that contained outliers were
679 removed.

680 Following pre-processing, peak-by-barcode matrices were processed as instructed by
681 Signac documentation: highly variable peaks were detected by Signac::FindTopFeatures() and
682 peak-by-barcode matrices normalized by Term Frequency - Inverse Document Frequency (TF-
683 IDF) method by Signac:: RunTFIDF().

684 To address batch specific variation, the integration framework from the Seurat package
685 was used on normalized peak-by-barcode matrices with the functions
686 Seurat::FindIntegrationAnchors(), which detects features common to all batches, and
687 Seurat::IntegrateEmbeddings(), which computes a weights matrix using the low dimensional cell
688 embeddings (LSI coordinates), prior to merging counts matrices across batches. All downstream
689 Seurat/Signac functions included "latent.vars" arguments to further regress out confounding
690 variables.

691 Following integration steps, dimensional reduction with Singular Value Decomposition
692 (SVD) and Uniform Manifold Approximation and Projection (UMAP), and cluster detection using
693 smart local moving (SLM) algorithm were performed. RNA cell type predictions from scRNA-Seq
694 were transferred to snATAC-Seq nuclei using the label transfer method outlined by Signac.
695 Following the standard Signac workflow, promoter accesbility (PA) for each gene was calculated
696 by summing all reads mapping to a gene body plus promoter (2 Kb upstream from gene TSSs).
697 Differential testing we performed for peak counts and PA by Seurat::FindAllMarkers(min.pct=0.2,
698 test.use='LR', latent.vars='nCount_peaks') and Seurat::FindAllMarkers(), respectively. Motif

699 analysis was performed using Signac by Seurat::FindMarkers(only.pos=TRUE, min.pct=0.2,
700 test.use='LR', latent.vars='nCount_peaks') followed by Signac::FindMotifs() and using the
701 JASPAR (http://jaspar.genereg.net/) CORE vertebrates collection as a reference database. Per
702 cell motif deviation scores were computed using chromVAR (v1.12.0) and the UCSC mm10
703 genome sequences (BSgenome.Mmusculus.UCSC.mm10, v1.4.0), both from Bioconductor
704 (v3.12), with the Signac::RunChromVAR() wrapper.

705 *Cicero*: Following outlier detection and dimensional reduction, the filtered peak-by-
706 barcode counts matrix was transferred from the Seurat object to a Monocle3 (https://cole-trapnell-
707 lab.github.io/monocle3/) cell_data_set (CDS) object. The counts object was processed with
708 Cicero (v1.9.1) (https://cole-trapnell-lab.github.io/cicero-release/) following user documentation
709 with defaults unless otherwise specified. Prior to calculating Cicero co-accessibility scores, a
710 Cicero CDS object was created using the newly created Monocle3 cds object and UMAP
711 coordinates from the Seurat object (i.e. cicero::make_cicero_cds(cds.object,
712 reduced_coordinates=seurat.object@reductions$umap@cell.embeddings)).

713 *SnapATAC*: snATAC-Seq reads were processed with SnapATAC (v1.0.0) independently
714 of Seurat/Signac/Cicero workflows following user documentation
715 (https://github.com/r3fang/SnapATAC) with default parameters unless otherwise specified.
716 FASTQ reads were converted into snap files using Snaptools (v1.4.1) and Python 2.7 and ATAC
717 accessible regions were binned into 5000 kB windows and counted to create cell-by-bin matrices.
718 Snap files were analyzed by SnapATAC. Valid cell barcodes with log10(UMI) between 3 to 6, and
719 promoter ratio between 0.05 to 0.6 were retained for further analysis. All other barcodes were
720 discarded. cell-by-bin matrices were merged, binarized, filtered against ENCODE blacklist
721 regions (http://mitra.stanford.edu/kundaje/akundaje/release/blacklists/), and barcodes with bin
722 counts less than 1000 and greater than the 95th percentile were removed. Dimensional reduction
723 was performed using Nyström landmark diffusion maps algorithm, batch reduction was performed
724 using Harmony (https://github.com/immunogenomics/harmony) by

725 SnapATAC::runHarmony(eigs.dim=1:40), a K Nearest Neighbor (KNN) graph constructed by
726 SnapATAC::runKNN(eigs.dims=1:dims_use, k=15) and the Louvain algorithm used to detect
727 clusters. Gene activity scores were calculated by counting snATAC-Seq reads mapping to known
728 gene bodies. scRNA-Seq/snRNA-Seq based cell type predictions were transferred to
729 corresponding snATAC-Seq barcodes by
730 SnapATAC::snapToSeurat(eigs.dims=1:40,norm=TRUE,scale=TRUE),
731 Seurat::FindTransferAnchors() and Seurat::TransferData() as described in SnapATAC
732 documentation. Cluster specific peaks were detected using MACS2 by
733 SnapATAC::runMACS(macs.options="--nomodel --shift 100 --ext 200 --qval 5e-2 -B --SPMR").
734 Gene-enhancer pairs were predicted by SnapATAC::predictGenePeakPair() for every TSS that
735 had a non-zero peak count across all barcodes. The gene-enhancer pairs list was filtered by
736 removing pairs where FDR > 0.05.

737 *Enhancer Prediction*: The greatest SnapATAC -log10(adjusted p-value) value was
738 multiplied by 2 as an upper limit, and all -log10(adjusted p-values) were percentile ranked per
739 gene. Similarly, Cicero co-accessibility scores were percentile ranked for each gene. Peaks
740 detected by SnapATAC or Cicero that did not overlap gene TSSs were extended 500 bp upstream
741 and downstream before merging overlapping peak coordinates using the GenomicRanges
742 (v1.42.0) Bioconductor package with GenomicRanges::reduce(). To generate a list of all
743 presumptive enhancers, merged SnapATAC peaks and merged Cicero peaks were
744 concatenated. To generate a more stringent list of enhancers for snATAC-Seq/scRNA-Seq
745 integration, the intersection SnapATAC and Cicero peaks was taken by
746 GenomicRanges::intersect(). To detect H3K27ac+ presumptive enhancers, concatenated peaks
747 were further filtered by retaining only peaks that intersected forebrain H3K27ac ChIP-Seq peaks
748 for age E12.5 (UCSC Database: mm10, Primary Table: encode3Ren_forebrain_H3K27ac_E12,
749 Big Bed File: /gbdb/mm10/encode3/histones/ENCFF957YEE.bigBed) or E14.5 (UCSC Database:
750 mm10, Primary Table: encode3Ren_forebrain_H3K27ac_E14, Big Bed File:

751 /gbdb/mm10/encode3/histones/ENCFF088LWR.bigBed) by
752 GenomicRanges::SubsetByOverlaps().
753
754 **scRNA-Seq/snATAC-Seq Analysis.** *scRNA-Seq/snATAC-Seq Integration*: For each data type,
755 barcodes were filtered to remove far-out outliers, as previously described by Tukey's fence
756 method. Prior to integrating data, for snATAC-Seq barcodes, gene activity score (GAS) was
757 calculated by counting reads that mapped to the promoter regions (2kb upstream of TSSs), the
758 first exon of each transcript, and (if detected) presumptive enhancer loci associated to each gene.
759 Integration of scRNA-Seq and snATAC-Seq datasets was performed using the Seurat integration
760 workflow. GAS (snATAC-Seq) and RNA (scRNA-Seq) count matrices were normalized with
761 Seurat::NormalizeData(), highly variable genes detected with Seurat::FindVariableFeatures() and
762 common features across all samples selected with Seurat::SelectIntegrationFeatures().
763 Integration of assays was performed with Seurat::FindIntegrationAnchors() and IntegrateData().
764 *degPatterns*: To obtain a list of differentially expressed genes (DEGs),
765 Seurat::FindMarkers() was used to detect DEGs from embryonic and P30 scRNA-Seq data.
766 Barcodes were ordered by increasing pseudotime, as assigned by Monocle3. The Seurat object
767 containing integrated snATAC-Seq/scRNA-Seq datasets was subset into 2 Seurat objects, one
768 containing scRNA-Seq and one containing snATAC-Seq. degPatterns were quantified using the
769 previously detected DEGs list and 3 separate matrices: gene-by-barcode counts (from scRNA-
770 Seq Seurat object), gene-by-barcode counts (GAS slot from snATAC-Seq Seurat object) and
771 gene-by-barcode counts (enhancer slot from snATAC-Seq Seurat object) by DEGReport::
772 degPatterns() using the DEGReport (https://github.com/lpantano/DEGreport) package.
773 *RNA/GAS/Enhancers Heatmaps*: The top 500 highly variable genes from embryonic
774 scRNA-Seq data were detected by Seurat::FindVariableFeatures(nfeatures = 500). Barcodes in
775 the Seurat object containing integrated snATAC-Seq/scRNA-Seq were ordered by increasing
776 pseudotime, as assigned by Monocle3. This Seurat object was subset into 2 Seurat objects, one

777 containing scRNA-Seq and one containing snATAC-Seq, which were further split into 3 matrices:
778 gene-by-barcode counts (from scRNA-Seq Seurat object), gene-by-barcode counts (GAS slot
779 from snATAC-Seq Seurat object) and gene-by-barcode counts (enhancer slot from snATAC-Seq
780 Seurat object). RNA, GAS and enhancer gene-by-barcode matrices were concatenated together,
781 and hierarchical clustering of genes was performed using correlation distance and average
782 linkage metrics. Following clustering, the concatenated matrix was re-split into RNA, GAS and
783 enhancer gene-by-barcode matrices. Matrices were centered and scaled for each gene prior to
784 rendering heatmaps and the gene dendrograms were constructed using the distances calculated
785 with the concatenated matrix. Manually annotated color bars were based on gene cohorts
786 detected by degPatterns().
787
788 **CUT&Tag Analysis.** Reads were aligned to mouse genome (GRCm38/mm10 build) with the
789 Bowtie2 aligner with the following parameters (-p 40 -N 1 --local --very-sensitive-local --no-unal -
790 -no-mixed --no-discordant --phred33 -I 10 -X 700), aligned reads mapping to blacklisted regions
791 were removed, and PCR duplicates were removed with PICARD. Quality control for replicates
792 was assessed using deepTools plotHeatmap and plotProfile, and reproducibility was assessed
793 by peak calling per replicate with MACS and calculating pair-wise consensus peak counts with
794 bedtools intersect using the parameter (-f 0.50). Replicates were merged with samtools merge,
795 deduplicated with PICARD, and peaks called with MACS using the parameter (--broad). To
796 generate signal tracks for visualization, the merged bam files were converted to normalized
797 bigWig files using deeptools bamCoverage with the following parameters (--normalizeUsing
798 RPKM -p 10 --binSize 5 --minFragmentLength 150).
799
800 **Hi-C and Capture-C analysis.** Hi-C and Capture-C libraries were sequenced with paired-end
801 reads of 51 nucleotides. Data was processed using the HiC-Pro pipeline[63] to produce a list of valid
802 interactions pairs. This list was converted into cool and mcool files for visualization with higlass[64].

For Capture-C data, the make_viewpoints Hicpro script was used to obtain individual Capture-C bigwig files for each replicate of each viewpoint with 2kb-sized bins and excluding 500bp surrounding the DpnII-fragment where probes hibridize. For visualization, averages from replicates were used.

Data Availability. Gene Expression Omnibus accession numbers for the sequencing data reported in the paper are GSE167047 (snATAC-Seq), GSE167013 (scRNA-Seq), GSEXXXXXX (H3K4me3 CUT&Tag), GSEXXXXXX (H3K27me3 CUT&Tag), GSEXXXXXX (H3K27ac CUT&RUN), GSEXXXXXX (Hi-C) and GSEXXXXXX (Capture-C). A searchable platform with all single cell accessibility and transcriptomic, CUT&Tag, CUT&Run, Hi-C and Capture-C data can be found on the UCSC Genome Browser: https://genome.ucsc.edu/cgi-bin/hgTracks?hubUrl=https://hpc.nih.gov/~BSPC-Petros/track_hub/chromatin_quantification.hub.txt&hgS_loadUrlName=https://hpc.nih.gov/~BSPC-Petros/track_hub/session.txt&hgS_doLoadUrl=submit.

835 **REFERENCES**

836

837 1 DeFelipe, J. *et al.* New insights into the classification and nomenclature of cortical
838 GABAergic interneurons. *Nat Rev Neurosci* **14**, 202-216, doi:10.1038/nrn3444 (2013).

839 2 Gouwens, N. W. *et al.* Integrated Morphoelectric and Transcriptomic Classification of
840 Cortical GABAergic Cells. *Cell* **183**, 935-953 e919, doi:10.1016/j.cell.2020.09.057
841 (2020).

842 3 Tasic, B. *et al.* Shared and distinct transcriptomic cell types across neocortical areas.
843 *Nature* **563**, 72-78, doi:10.1038/s41586-018-0654-5 (2018).

844 4 Bandler, R. C., Mayer, C. & Fishell, G. Cortical interneuron specification: the juncture of
845 genes, time and geometry. *Curr Opin Neurobiol* **42**, 17-24,
846 doi:10.1016/j.conb.2016.10.003 (2017).

847 5 Pelkey, K. A. *et al.* Hippocampal GABAergic Inhibitory Interneurons. *Physiol Rev* **97**,
848 1619-1747, doi:10.1152/physrev.00007.2017 (2017).

849 6 Miyoshi, G. Elucidating the developmental trajectories of GABAergic cortical interneuron
850 subtypes. *Neurosci Res* **138**, 26-32, doi:10.1016/j.neures.2018.09.012 (2019).

851 7 Lui, J. H., Hansen, D. V. & Kriegstein, A. R. Development and evolution of the human
852 neocortex. *Cell* **146**, 18-36, doi:10.1016/j.cell.2011.06.030 (2011).

853 8 Mayer, C. *et al.* Developmental diversification of cortical inhibitory interneurons. *Nature*
854 **555**, 457-462, doi:10.1038/nature25999 (2018).

855 9 Mi, D. *et al.* Early emergence of cortical interneuron diversity in the mouse embryo.
856 *Science* **360**, 81-85, doi:10.1126/science.aar6821 (2018).

857 10 Fishell, G. & Kepecs, A. Interneuron Types as Attractors and Controllers. *Annu Rev*
858 *Neurosci* **43**, 1-30, doi:10.1146/annurev-neuro-070918-050421 (2020).

859 11 Bandler, R. C. *et al.* Single-cell delineation of lineage and genetic identity in the mouse
860 brain. *Nature*, doi:10.1038/s41586-021-04237-0 (2021).

861 12 Podobinska, M. *et al.* Epigenetic Modulation of Stem Cells in Neurodevelopment: The
862 Role of Methylation and Acetylation. *Front Cell Neurosci* **11**, 23,
863 doi:10.3389/fncel.2017.00023 (2017).

864 13 Sokpor, G., Castro-Hernandez, R., Rosenbusch, J., Staiger, J. F. & Tuoc, T. ATP-
865 Dependent Chromatin Remodeling During Cortical Neurogenesis. *Front Neurosci* **12**,
866 226, doi:10.3389/fnins.2018.00226 (2018).

867 14 Dall'Aglio, L. *et al.* The role of epigenetic modifications in neurodevelopmental disorders:
868 A systematic review. *Neurosci Biobehav Rev* **94**, 17-30,
869 doi:10.1016/j.neubiorev.2018.07.011 (2018).

15 Sokpor, G., Xie, Y., Rosenbusch, J. & Tuoc, T. Chromatin Remodeling BAF (SWI/SNF) Complexes in Neural Development and Disorders. *Front Mol Neurosci* **10**, 243, doi:10.3389/fnmol.2017.00243 (2017).

16 Wang, D. *et al.* Comprehensive functional genomic resource and integrative model for the human brain. *Science* **362**, doi:10.1126/science.aat8464 (2018).

17 Cross-Disorder Group of the Psychiatric Genomics Consortium, C. Genomic Relationships, Novel Loci, and Pleiotropic Mechanisms across Eight Psychiatric Disorders. *Cell* **179**, 1469-1482 e1411, doi:10.1016/j.cell.2019.11.020 (2019).

18 Grove, J. *et al.* Identification of common genetic risk variants for autism spectrum disorder. *Nat Genet* **51**, 431-444, doi:10.1038/s41588-019-0344-8 (2019).

19 Schork, A. J. *et al.* A genome-wide association study of shared risk across psychiatric disorders implicates gene regulation during fetal neurodevelopment. *Nat Neurosci* **22**, 353-361, doi:10.1038/s41593-018-0320-0 (2019).

20 Trevino, A. E. *et al.* Chromatin accessibility dynamics in a model of human forebrain development. *Science* **367**, doi:10.1126/science.aay1645 (2020).

21 Carullo, N. V. N. & Day, J. J. Genomic Enhancers in Brain Health and Disease. *Genes (Basel)* **10**, doi:10.3390/genes10010043 (2019).

22 Kikuchi, M. *et al.* Enhancer variants associated with Alzheimer's disease affect gene expression via chromatin looping. *BMC Med Genomics* **12**, 128, doi:10.1186/s12920-019-0574-8 (2019).

23 Perenthaler, E., Yousefi, S., Niggl, E. & Barakat, T. S. Beyond the Exome: The Non-coding Genome and Enhancers in Neurodevelopmental Disorders and Malformations of Cortical Development. *Front Cell Neurosci* **13**, 352, doi:10.3389/fncel.2019.00352 (2019).

24 Buenrostro, J. D., Wu, B., Chang, H. Y. & Greenleaf, W. J. ATAC-seq: A Method for Assaying Chromatin Accessibility Genome-Wide. *Curr Protoc Mol Biol* **109**, 21 29 21-21 29 29, doi:10.1002/0471142727.mb2129s109 (2015).

25 Waltman, L. & van Eck, N. J. A smart local moving algorithm for large-scale modularity-based community detection. *Eur Phys J B* **86**, 471, doi:10.1140/epjb/e2013-40829-0 (2013).

26 Wullimann, M. F. Should we redefine the classic lateral pallium? *J Comp Neurol* **525**, 1509-1513, doi:10.1002/cne.24127 (2017).

27 Moreau, M. X., Saillour, Y., Cwetsch, A. W., Pierani, A. & Causeret, F. Single-cell transcriptomics of the early developing mouse cerebral cortex disentangle the spatial and temporal components of neuronal fate acquisition. *Development* **148**, doi:10.1242/dev.197962 (2021).

28 Cao, J. *et al.* The single-cell transcriptional landscape of mammalian organogenesis. *Nature* **566**, 496-502, doi:10.1038/s41586-019-0969-x (2019).

908 29 Trapnell, C. *et al.* The dynamics and regulators of cell fate decisions are revealed by
909 pseudotemporal ordering of single cells. *Nat Biotechnol* **32**, 381-386,
910 doi:10.1038/nbt.2859 (2014).

911 30 Lothian, C. & Lendahl, U. An evolutionarily conserved region in the second intron of the
912 human nestin gene directs gene expression to CNS progenitor cells and to early neural
913 crest cells. *Eur J Neurosci* **9**, 452-462, doi:10.1111/j.1460-9568.1997.tb01622.x (1997).

914 31 Preissl, S. *et al.* Single-nucleus analysis of accessible chromatin in developing mouse
915 forebrain reveals cell-type-specific transcriptional regulation. *Nat Neurosci* **21**, 432-439,
916 doi:10.1038/s41593-018-0079-3 (2018).

917 32 Maybury-Lewis, S. Y. *et al.* Changing and stable chromatin accessibility supports
918 transcriptional overhaul during neural stem cell activation. *bioRxiv* (2020).

919 33 Stergachis, A. B. *et al.* Developmental fate and cellular maturity encoded in human
920 regulatory DNA landscapes. *Cell* **154**, 888-903, doi:10.1016/j.cell.2013.07.020 (2013).

921 34 Khan, A. *et al.* JASPAR 2018: update of the open-access database of transcription
922 factor binding profiles and its web framework. *Nucleic Acids Res* **46**, D260-D266,
923 doi:10.1093/nar/gkx1126 (2018).

924 35 Schep, A. N., Wu, B., Buenrostro, J. D. & Greenleaf, W. J. chromVAR: inferring
925 transcription-factor-associated accessibility from single-cell epigenomic data. *Nat*
926 *Methods* **14**, 975-978, doi:10.1038/nmeth.4401 (2017).

927 36 Hu, J. S. *et al.* Coup-TF1 and Coup-TF2 control subtype and laminar identity of MGE-
928 derived neocortical interneurons. *Development* **144**, 2837-2851, doi:10.1242/dev.150664
929 (2017).

930 37 Pliner, H. A. *et al.* Cicero Predicts cis-Regulatory DNA Interactions from Single-Cell
931 Chromatin Accessibility Data. *Mol Cell* **71**, 858-871 e858,
932 doi:10.1016/j.molcel.2018.06.044 (2018).

933 38 Kanatani, S., Yozu, M., Tabata, H. & Nakajima, K. COUP-TFII is preferentially expressed
934 in the caudal ganglionic eminence and is involved in the caudal migratory stream. *J*
935 *Neurosci* **28**, 13582-13591, doi:10.1523/JNEUROSCI.2132-08.2008 (2008).

936 39 Ma, T. *et al.* A subpopulation of dorsal lateral/caudal ganglionic eminence-derived
937 neocortical interneurons expresses the transcription factor Sp8. *Cereb Cortex* **22**, 2120-
938 2130, doi:10.1093/cercor/bhr296 (2012).

939 40 Fang, R. *et al.* Fast and Accurate Clustering of Single Cell Epigenomes Reveals Cis-
940 Regulatory Elements in Rare Cell Types. *bioRxiv*, doi:10.1101/615179 (2019).

941 41 Gorkin, D. U. *et al.* An atlas of dynamic chromatin landscapes in mouse fetal
942 development. *Nature* **583**, 744-751, doi:10.1038/s41586-020-2093-3 (2020).

943 42 Visel, A., Minovitsky, S., Dubchak, I. & Pennacchio, L. A. VISTA Enhancer Browser--a
944 database of tissue-specific human enhancers. *Nucleic Acids Res* **35**, D88-92,
945 doi:10.1093/nar/gkl822 (2007).

946 43 Pantano, L. DEGreport: Report of DEG analysis. R package version 1.13.8.,
947 doi:10.18129/B9.bioc.DEGreport (2017).

948 44 Skene, P. J. & Henikoff, S. An efficient targeted nuclease strategy for high-resolution
949 mapping of DNA binding sites. *Elife* **6**, doi:10.7554/eLife.21856 (2017).

950 45 Kaya-Okur, H. S. *et al.* CUT&Tag for efficient epigenomic profiling of small samples and
951 single cells. *Nat Commun* **10**, 1930, doi:10.1038/s41467-019-09982-5 (2019).

952 46 Hughes, A. L., Kelley, J. R. & Klose, R. J. Understanding the interplay between CpG
953 island-associated gene promoters and H3K4 methylation. *Biochim Biophys Acta Gene*
954 *Regul Mech* **1863**, 194567, doi:10.1016/j.bbagrm.2020.194567 (2020).

955 47 Calo, E. & Wysocka, J. Modification of enhancer chromatin: what, how, and why? *Mol*
956 *Cell* **49**, 825-837, doi:10.1016/j.molcel.2013.01.038 (2013).

957 48 Schuettengruber, B., Bourbon, H. M., Di Croce, L. & Cavalli, G. Genome Regulation by
958 Polycomb and Trithorax: 70 Years and Counting. *Cell* **171**, 34-57,
959 doi:10.1016/j.cell.2017.08.002 (2017).

960 49 Tucker, E. S. *et al.* Molecular specification and patterning of progenitor cells in the lateral
961 and medial ganglionic eminences. *J Neurosci* **28**, 9504-9518,
962 doi:10.1523/JNEUROSCI.2341-08.2008 (2008).

963 50 Markenscoff-Papadimitriou, E. *et al.* A Chromatin Accessibility Atlas of the Developing
964 Human Telencephalon. *Cell* **182**, 754-769 e718, doi:10.1016/j.cell.2020.06.002 (2020).

965 51 Ziffra, R. S. *et al.* Single cell epigenomic atlas of the developing human brain and
966 organoids. *bioRxiv* (2019).

967 52 Allaway, K. C. *et al.* Genetic and epigenetic coordination of cortical interneuron
968 development. *Nature* **597**, 693-697, doi:10.1038/s41586-021-03933-1 (2021).

969 53 Ma, S. *et al.* Chromatin Potential Identified by Shared Single-Cell Profiling of RNA and
970 Chromatin. *Cell* **183**, 1103-1116 e1120, doi:10.1016/j.cell.2020.09.056 (2020).

971 54 Schmitt, A. D. *et al.* A Compendium of Chromatin Contact Maps Reveals Spatially Active
972 Regions in the Human Genome. *Cell Rep* **17**, 2042-2059,
973 doi:10.1016/j.celrep.2016.10.061 (2016).

974 55 Winick-Ng, W. *et al.* Cell-type specialization is encoded by specific chromatin topologies.
975 *Nature* **599**, 684-691, doi:10.1038/s41586-021-04081-2 (2021).

976 56 Javierre, B. M. *et al.* Lineage-Specific Genome Architecture Links Enhancers and Non-
977 coding Disease Variants to Target Gene Promoters. *Cell* **167**, 1369-1384 e1319,
978 doi:10.1016/j.cell.2016.09.037 (2016).

979 57 Webb, M. R., Hibberd, M. G., Goldman, Y. E. & Trentham, D. R. Oxygen exchange
980 between Pi in the medium and water during ATP hydrolysis mediated by skinned fibers
981 from rabbit skeletal muscle. Evidence for Pi binding to a force-generating state. *J Biol*
982 *Chem* **261**, 15557-15564 (1986).

58 Bonev, B. *et al.* Multiscale 3D Genome Rewiring during Mouse Neural Development. *Cell* **171**, 557-572 e524, doi:10.1016/j.cell.2017.09.043 (2017).

59 Ghavi-Helm, Y. *et al.* Enhancer loops appear stable during development and are associated with paused polymerase. *Nature* **512**, 96-100, doi:10.1038/nature13417 (2014).

60 Ing-Simmons, E. *et al.* Independence of chromatin conformation and gene regulation during Drosophila dorsoventral patterning. *Nat Genet* **53**, 487-499, doi:10.1038/s41588-021-00799-x (2021).

61 Lee, D. R. *et al.* Transcriptional heterogeneity of ventricular zone cells throughout the embryonic mouseforebrain. *bioRxiv*, doi:doi.org/10.1101/2021.07.05.451224 (2021).

62 Thompson, J. J. *et al.* Rapid redistribution and extensive binding of NANOG and GATA6 at shared regulatory elements underlie specification of divergent cell fates. *bioRxiv*, 2021.2007.2028.454132, doi:10.1101/2021.07.28.454132 (2021).

63 Servant, N. *et al.* HiC-Pro: an optimized and flexible pipeline for Hi-C data processing. *Genome Biol* **16**, 259, doi:10.1186/s13059-015-0831-x (2015).

64 Kerpedjiev, P. *et al.* HiGlass: web-based visual exploration and analysis of genome interaction maps. *Genome Biol* **19**, 125, doi:10.1186/s13059-018-1486-1 (2018).

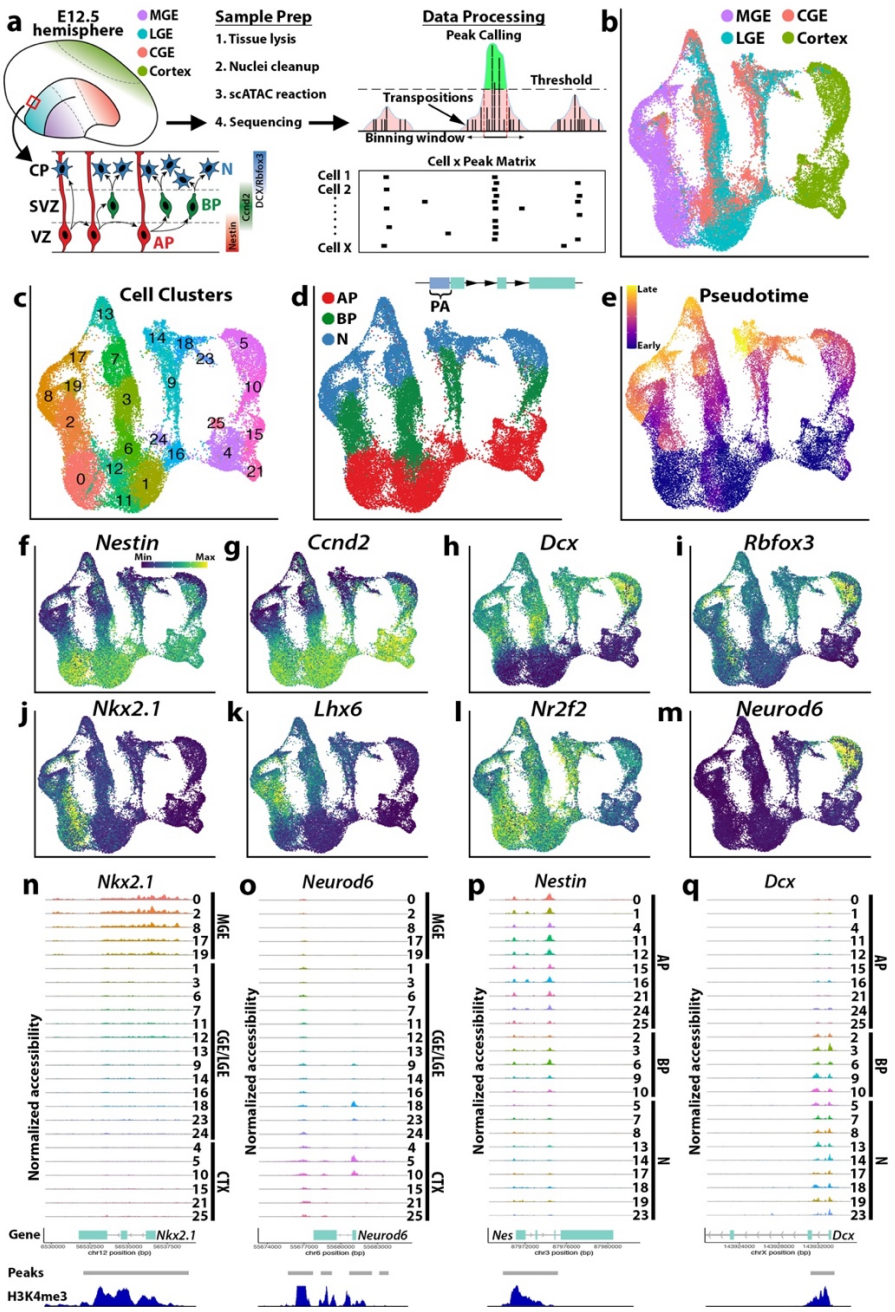

Fig 1. Chromatin accessibility in the embryonic forebrain is cell type and state specific. a, Schematic of snATAC-Seq workflow and neurogenic cell types: apical progenitors (APs), basal progenitors (BPs) and neurons (Ns). **b-e,** UMAP visualization of single nuclei clustered by brain region (**b**), SLM (**c**), neurogenic cell type (**d**) and pseudotime (**e**). In **d**, PA = promoter accessibility, representing reads mapping within 2 kb upstream of TSSs. **f-m**, PA scores for genes enriched in specific neurogenic cell types (**f-i**) or distinct brain regions (**j-m**). **n-q**, Aggregated reads per SLM cluster. *Nkx2-1* (MGE), *Neurod6* (cortex), *Nes* (APs) and *Dcx* (BPs/Ns), arranged by either brain region (**n-o**) or neurogenic cell type (**p-q**). The y-axis range for chromatin accessibility tracks are normalized to the maximum reads per gene. Peaks: differentially accessible peak coordinates, H3K4me3: H3K4me3 signal from E12.5 forebrain ENCODE ChIP-Seq data.

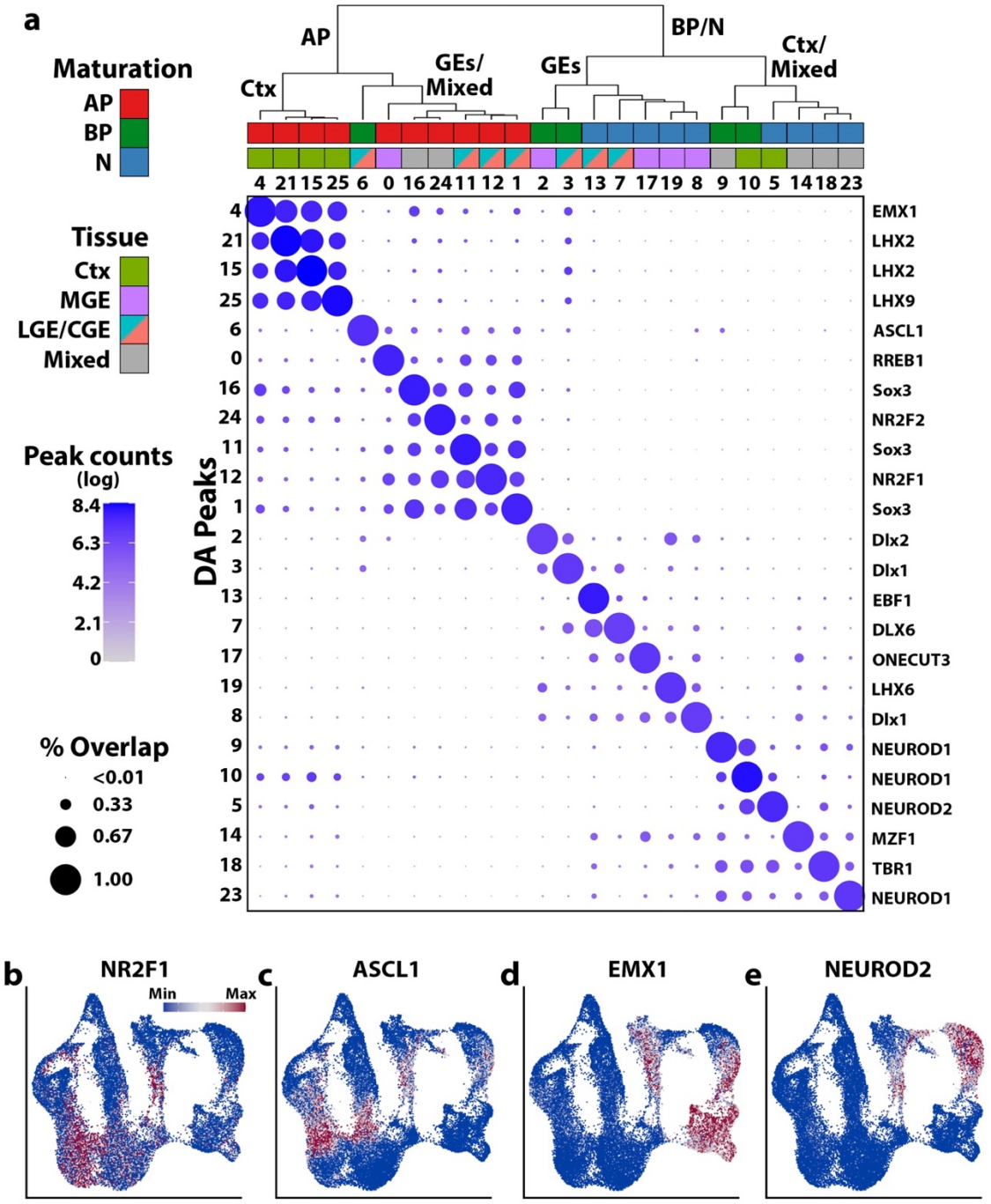

Fig 2. Differentially accessible peaks are cluster and lineage specific. a, Embryonic snATAC-Seq dot plot of differentially accessible peaks (DA peaks) for each cluster. Dot diameter indicates the percent of DA peaks from one cluster (column cluster labels) which are detectable in any other cluster (row cluster labels). Color intensity represents the total DA peak count per cluster. Hierarchical clustering was performed using correlation distance and average linkage. Names of representative cluster-enriched transcription factor binding motifs in DA peaks listed to right of dot plot. **b-e**, UMAP plots of nuclei colored by ChromVAR global motif deviations (Z-scores) for NR2F1, ASCL1, EMX1 and NEUROD2.

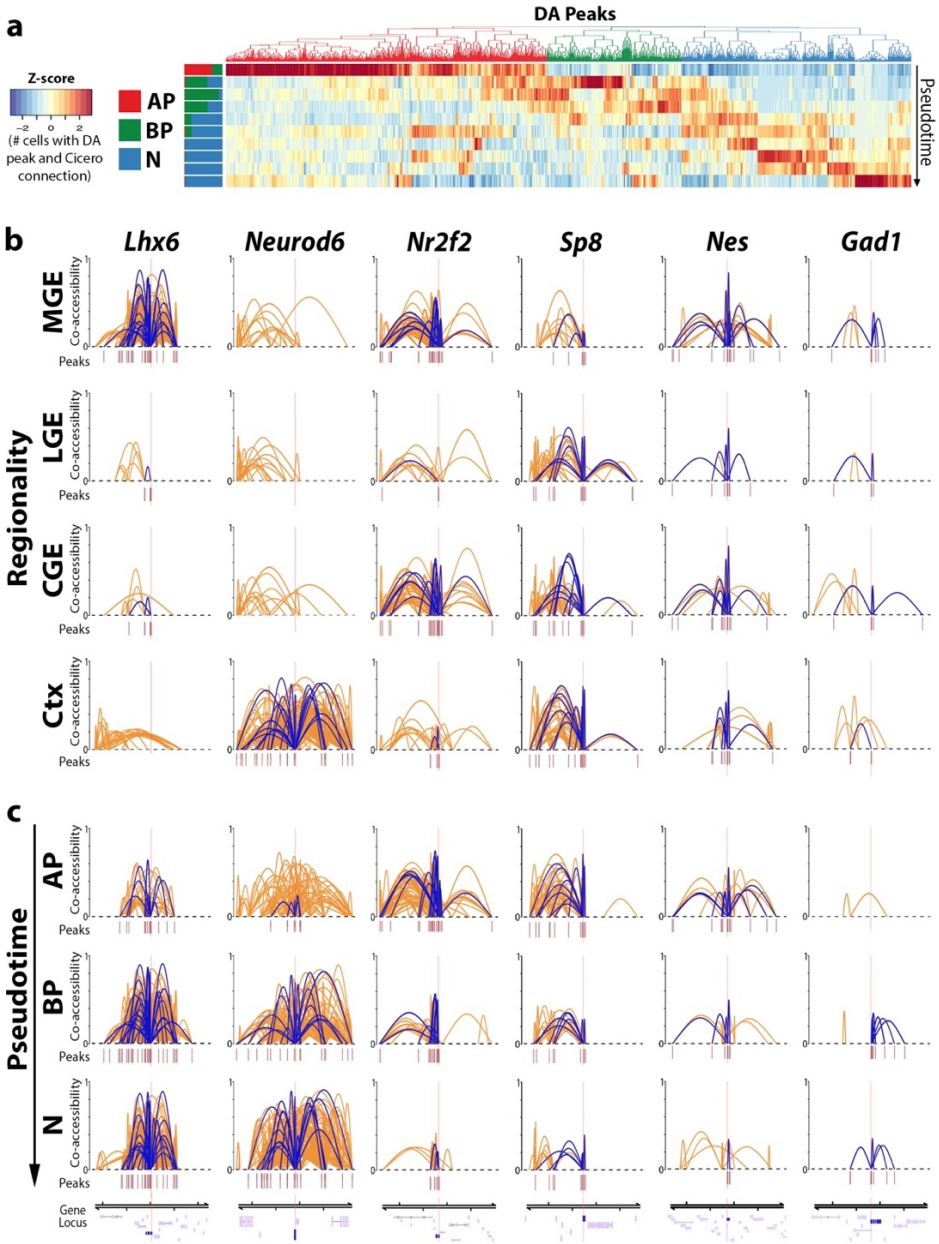

Fig. 3. Detection of cis-regulatory elements within the developing mouse forebrain. a, Heatmap depicting DA peaks binned along pseudotime from embryonic snATAC-Seq nuclei. DA peaks were filtered to retain only peaks that had at least one Cicero peak-peak connection. Stacked bar plots to left of heatmap depicts proportion of AP, BP and N nuclei per bin. **b-c**, Cicero connections within 0.5 Mb window centered around TSS of *Lhx6* (postmitotic MGE marker), *Neurod6* (postmitotic cortex marker), *Nr2f2* (CGE progenitors), *Sp8* (LGE progenitors), *Nes* (pan-AP) and *Gad1* (pan-interneuron) broken down based on tissue (**b**) or neurogenic cell type (**c**). Cicero connections overlapping the TSS of selected genes shown as purple arcs, all Cicero connections in genomic region shown as orange arcs. Y-axis unit is co-accessibility score. Only connections with co-accessibility scores greater than 0.25 are depicted. Peaks: snATAC peaks used by Cicero to quantify peak-peak connections. Gene models are visualized at the bottom of each column with gene of interest highlighted.

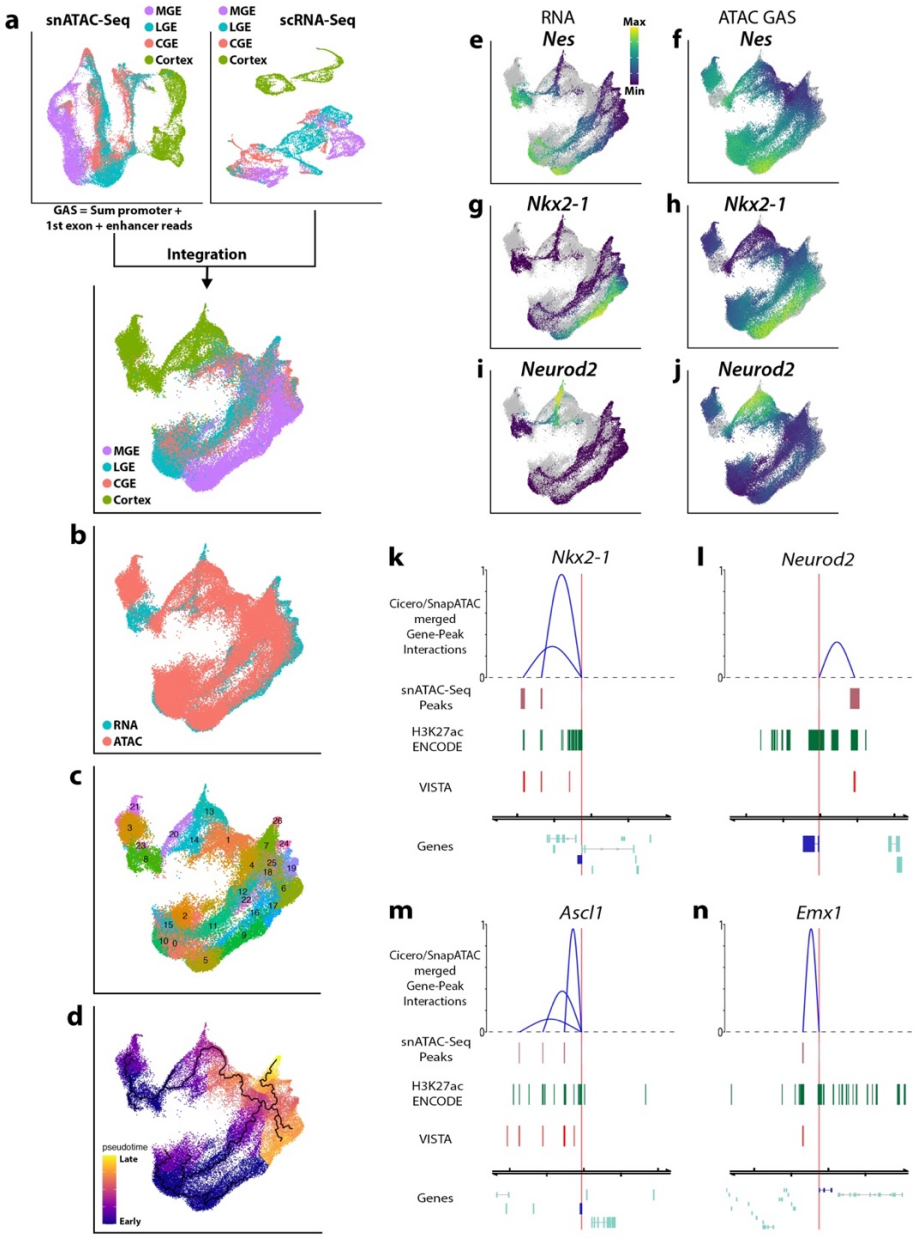

Fig. 4. Integrative analysis of embryonic snATAC-Seq and scRNA-Seq. a, Workflow depicting integration of embryonic snATAC-Seq (top left) and scRNA-Seq (top right) data. Bottom, UMAP plot showing integrated snATAC-Seq nuclei and scRNA-Seq cells colored by tissue. **b-d**, UMAP visualization of integrated snATAC-Seq/scRNA-Seq data colored by assay (**b**), Louvain cluster (**c**), and pseudotime (**d**). **e-j**, UMAP visualization of integrated scRNA-Seq cells and snATAC-sec nuclei colored by transcript counts or GAS for *Nes* (**e-f**), *Nkx2-1* (**g-h**) and *Neurod2* (**i-j**). Grey dots in background represent cells/nuclei from other assay. **k-m**, Genome browser tracks displaying enhancer predictions regulating *Nkx2-1* (**k**), *Neurod2* (**l**), *Ascl1* (**m**) and *Emx1* (**n**). Gene-Peak interactions are visualized in blue arcs, arc heights indicate the relative interaction scores between gene TSS (red line) and peaks. snATAC-Seq Peaks: displays co-accessible coordinates, H3K27ac ENCODE: Forebrain E12.5 H3K27ac peaks from ENCODE project, VISTA: enhancers from the VISTA Genome Browser project.

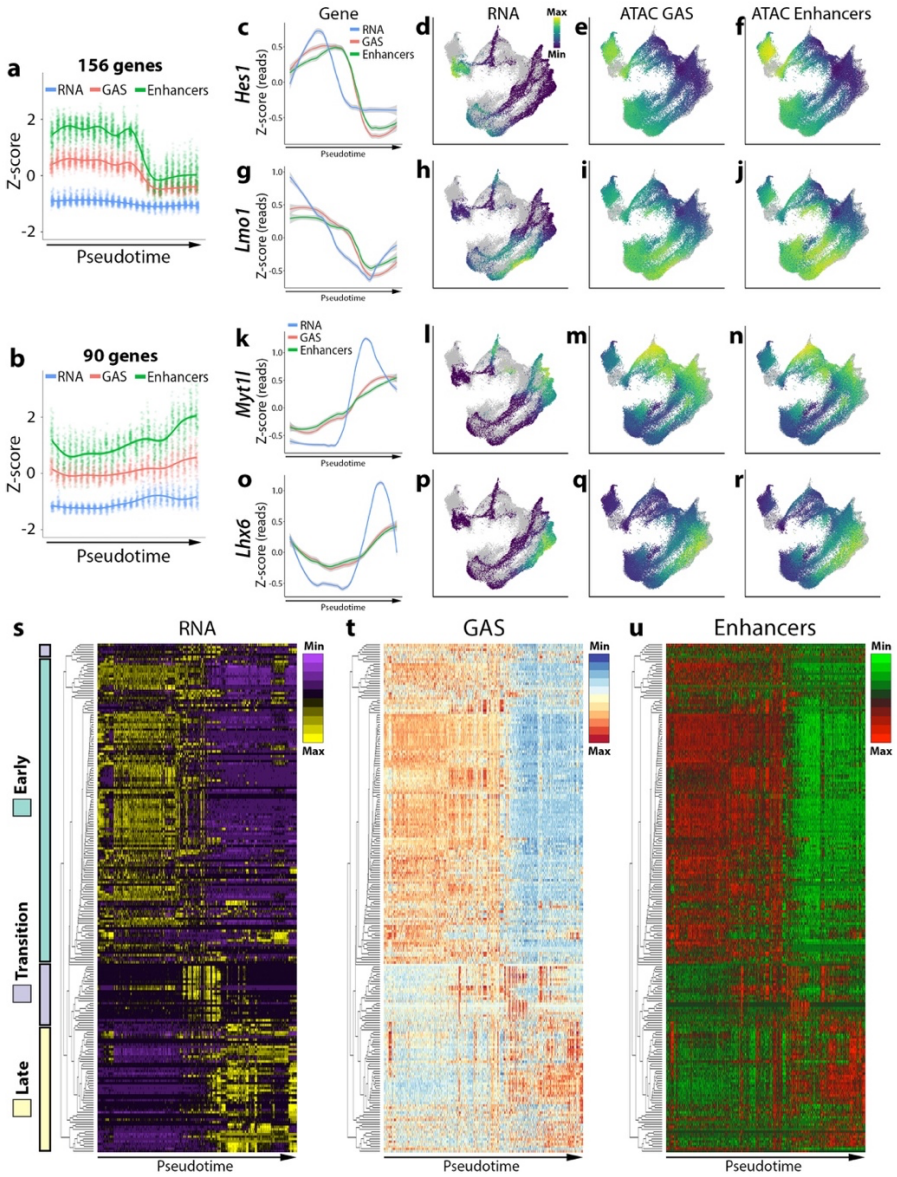

Fig. 5. Transcription, gene accessibility and active enhancer utilization are highly correlated and dynamic during neuron lineage commitment. a-b, Line charts of 'early expressed' (**a**) and 'late expressed' (**b**) DEG clusters detected by degPatterns using embryonic integrated snATAC-Seq/scRNA-Seq data. Y-axis is Z-score for RNA, GAS, or enhancers counts per gene. X-axis is binned pseudotime periods. RNA, GAS, or enhancers for individual genes in these clusters are plotted (156 'early' and 90 'late' genes). **c-r**, Line chart and UMAP visualizations of RNA, GAS and enhancer read counts for representative 'early' genes *Hes1* and *Lmo1* (**c-j**) and 'late' genes *Myt1l* and *Lhx6* (**k-r**). For line charts, Y-axis is Z-score for RNA, GAS, or enhancers counts per gene. X-axis is binned pseudotime periods. Grey dots in background of UMAP plots represent cells/nuclei from other assay. **s-u**, Heatmaps of RNA (**s**), GAS (**t**) and enhancers (**u**) counts for 210 variable genes. Heatmap columns were ordered by hierarchical clustering of 210 variable genes with correlation distance and average linkage. Rows were ordered by pseudotime (assigned by Moncole3). Color bars in **s** indicate genes grouped together based on 'early', 'transition' and 'late' profiles (as assigned by degPatterns and manually refined).

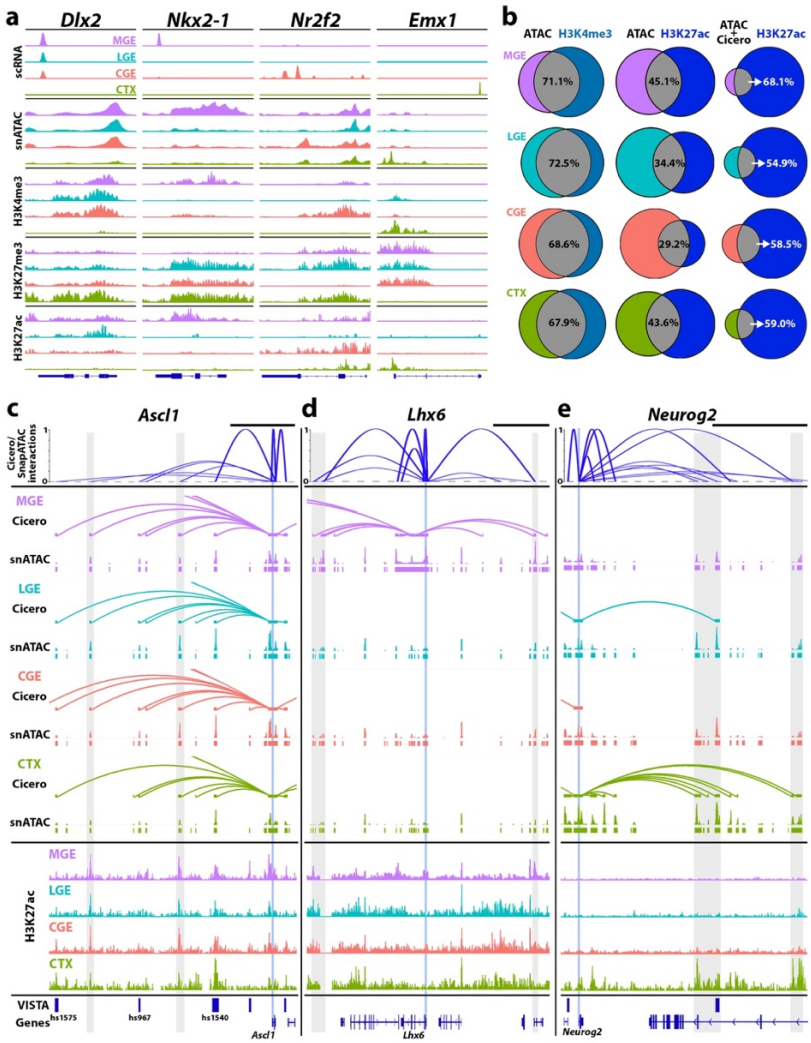

Fig. 6. Histone modifications within embryonic neural progenitors. a, Tracks of scRNA-Seq, snATAC-Seq and histone modifications correlated with active promoters (H3K4me3), repressed genes (H3K27me3) and active enhancers (H3K27ac) in MGE, LGE, CGE and cortex (CTX); pan-GE *Dlx2*, MGE-restricted *Nkx2-1*, CGE-enriched *Nr2f2* and cortex-restricted *Emx1*. **b**, Venn diagrams comparing ATAC peaks at promoter regions vs. H3K4me3 peaks at promoters (left); ATAC peaks outside promoters vs. H3K27ac peaks outside promoters (middle); and ATAC peaks with Cicero connections to a gene promoter vs. H3K27ac peaks outside promoters. Percentages represent % of ATAC peaks overlapping with histone marks per brain region. **c-e**, Top, Integration of gene-enhancer predictions using Cicero/SnapATAC interactions as in Extended Figure 6. Arc height of Cicero/SnapATAC interactions track indicates relative interaction scores between gene TSS and predicted cis-regulatory elements. Middle, tissue-specific Cicero connections with snATAC peaks. Cicero connections were filtered to retain scores > 0.25, and connections where one anchor intersects a gene TSS while the second anchor does not intersect promoter regions of any genes. Bottom, H3K27ac tracks with VISTA hits for *Ascl1* (**c**), *Lhx6* (**d**) and *Neurog2* (**e**). Vertical blue line denotes TSS for each gene, grey shaded rectangles indicate loci of interest related to TSS. VISTA hits near genes are depicted with dark blue bars. Black scale bars above Cicero/SnapATAC tracks = 50 kb.

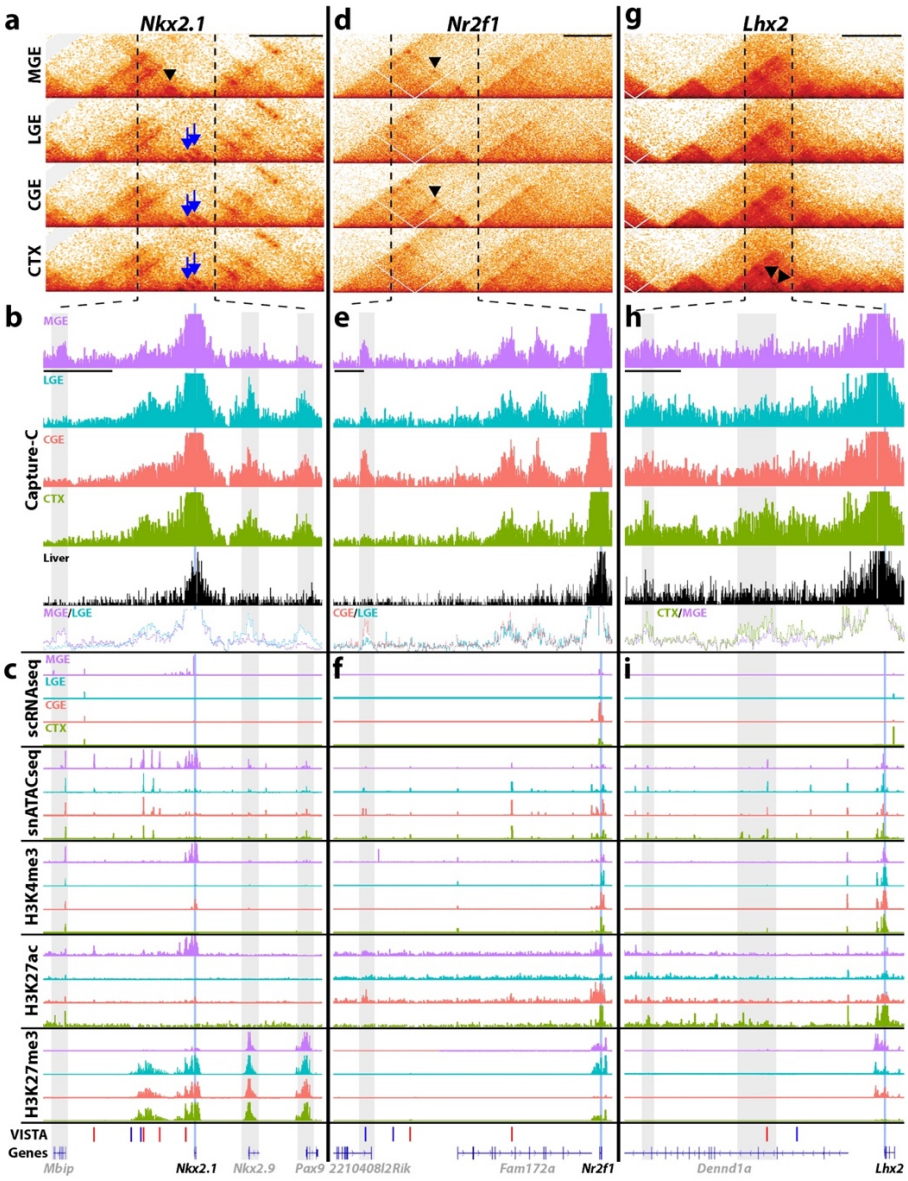

Fig. 7. Higher-order chromatin structure within embryonic neural progenitors. a, Hi-C 1D interaction frequency heatmaps for MGE, LGE, CGE and CTX at MGE-restricted *Nkx2-1*. Black triangle denotes an MGE-specific interaction, blue arrows denote non-MGE specific interactions. **b**, Capture-C pileup at *Nkx2-1* locus extending to vertical dashed lines in **a**. Y-axis represents reads from loci interacting with *Nkx2-1* promoter bait. Blue line indicates gene TSS, grey bars indicate potential regulatory elements directly interacting with *Nkx2-1* promoter. **c**, Signal tracks for single cell assays (scRNA-Seq and snATAC-Seq) and histone modifications correlated with active promoters (H3K4me3), active enhancers (H3K27ac) and repressed genes (H3K27me3) in each tissue. VISTA track includes tested enhancers. **d-f**, Hi-C heatmaps (**d**), Capture-C interactions (**e**) and chromatin landscape (**f**) of CGE-enriched *Nr2f1*. Black triangles in **d** denote MGE and CGE-enriched interactions. **g-i**, Hi-C heatmaps (**g**), Capture-C interactions (**h**) and chromatin landscape (**i**) of cortex-restricted *Lhx2*. Black triangles in **g** denote CTX-enriched interactions. Black scale bars above Hi-C plots in **a**, **d**, **g** = 500 kb, black scale bars below MGE Capture-C tracks in **b**, **e**, **h** = 100 kb.

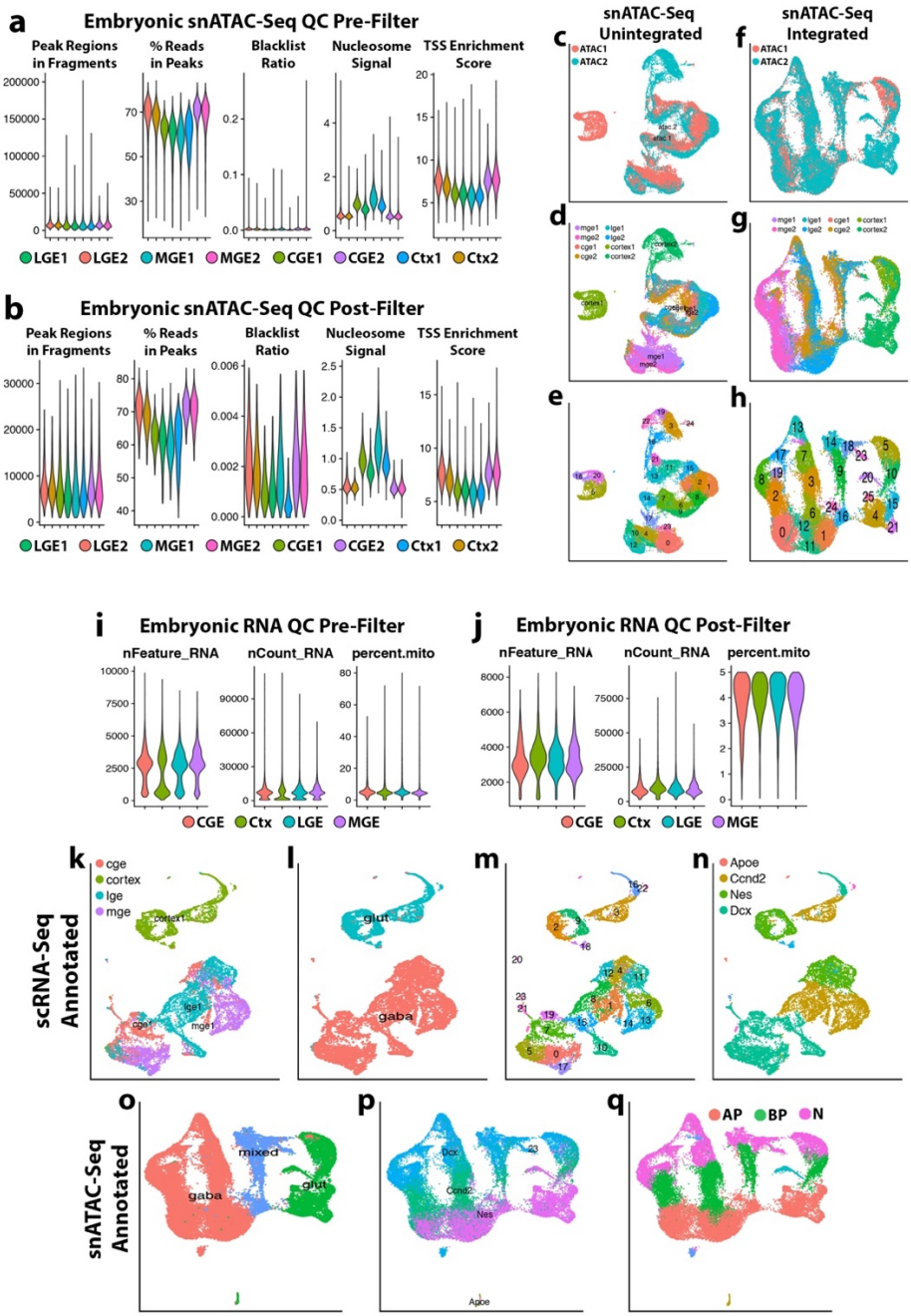

Extended Data Fig 1. snATAC-Seq and scRNA-Seq quality control and batch reduction, and scRNA-Seq based snATAC-Seq annotation. a, Violin plots of snATAC-Seq QC metrics before outlier removal. **b**, Violin plots of snATAC-Seq QC metrics after outlier removal. **c-e**, UMAP visualization of snATAC-Seq nuclei prior to batch removal colored by replicate (**c**), tissue origin (**d**) and SLM cluster (**e**). **f-h**, UMAP visualization of batch corrected snATAC-Seq nuclei colored by replicate (**f**), tissue origin (**g**) and SLM cluster (**h**). **i**, Violin plots of scRNA-Seq QC metrics before outlier removal. **j**, Violin plots of scRNA -Seq QC metrics after outlier removal. **k-n**, UMAP visualization of scRNA-Seq cells colored by tissue (**k**), neuronal class (**l**), Louvain cluster (**m**) and cell type (**n**). **o-q**, UMAP visualization of snATAC-Seq nuclei colored by neuronal class (**o**), scRNA-Seq cell type predictions (**p**) and assigned neurogenic cell type (**q**).

Extended Data Fig. 2. Visualization of GAS for critical interneuron markers. UMAP visualization of GAS from snATAC-Seq nuclei for specified genes. Legend depicts normalized read counts.

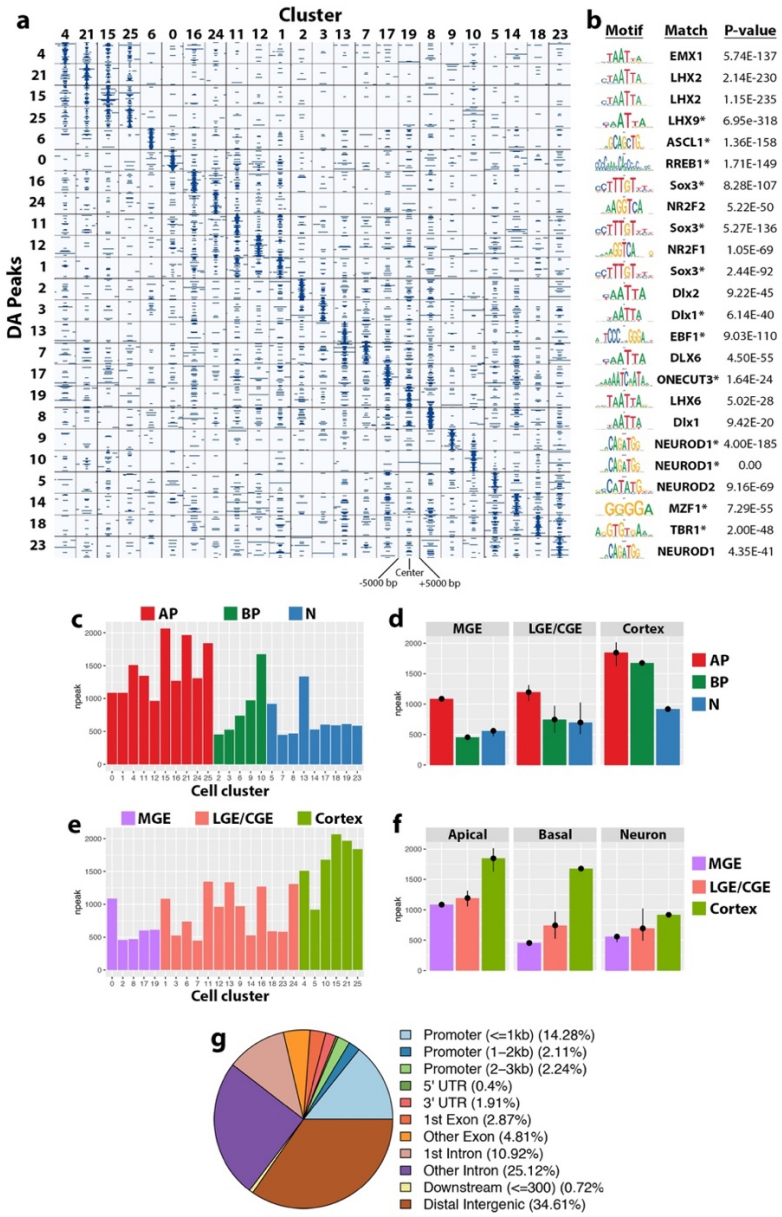

Extended Data Fig. 3. DA Peaks per cluster and read distribution across gene features. a, Embryonic snATAC-Seq signal plots of DA peaks for each cluster (same cluster order as Fig 2). Signal was binarized to indicate DA peaks from one cluster (column cluster labels) which are detectable in any other cluster (row cluster labels). **b**, For each cluster (rows of the dot plot), motifs representative of lineage and maturation stage, corresponding motif name and P-value are displayed to the right of the dot plot. All motifs are in the top five hits for each cluster, with top hits indicated with an asterisk. **c**, Bar chart of DA peak counts where -log(Fold Change) > 0 per SLM cluster colored by neurogenic cell type. **d**, Bar graph of mean DA peak counts where -log(Fold Change) > 0 per SLM cluster colored by neurogenic cell type and grouped by tissue. **e**, Bar chart of DA peak counts where -log(Fold Change) > 0 per SLM cluster colored by tissue. **f**, Bar chart of mean DA peak counts where -log(Fold Change) > 0 per SLM cluster colored by tissue and grouped by neurogenic cell type. **G**, Pie chart of relative enrichment of DA peaks within annotated gene features.

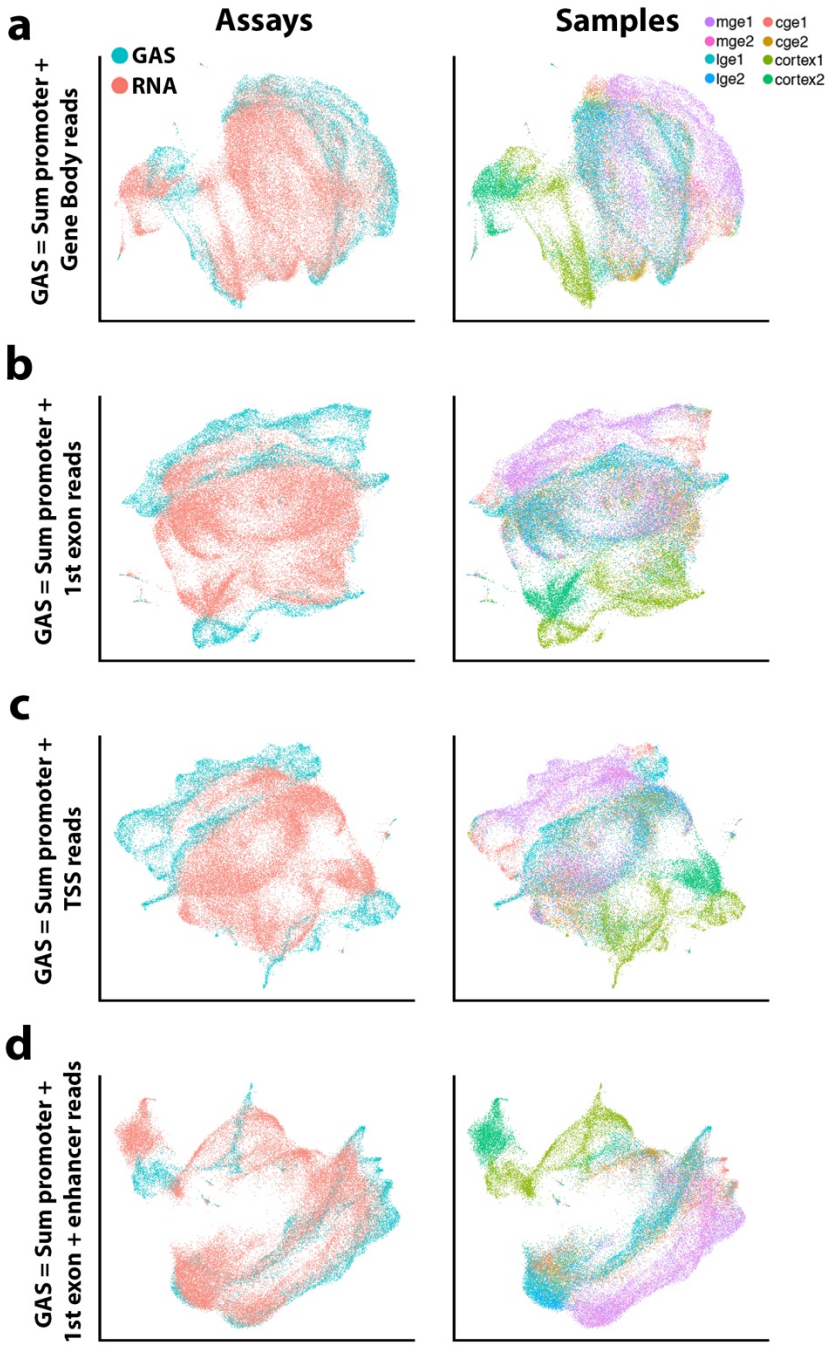

Extended Data Fig. 4. Gene activity score comparisons. UMAP visualizations of integrated snATAC-Seq and scRNA-Seq data colored by assay (left) and tissue samples (right). For integration, snATAC-Seq Gene Activity Score (GAS) was quantified using four different strategies: (**a**) quantified peaks within gene promoters (-2000 bp to 0 bp of 5' transcript coordinate) and gene bodies, (**b**) quantified peaks within gene promoters and the first exon of all transcripts, (**c**) quantified peaks within gene promoters only, and (**d**) quantified peaks within promoters, the first exon of all transcripts, and any associated putative enhancers (H3K27ac+ chromatin).

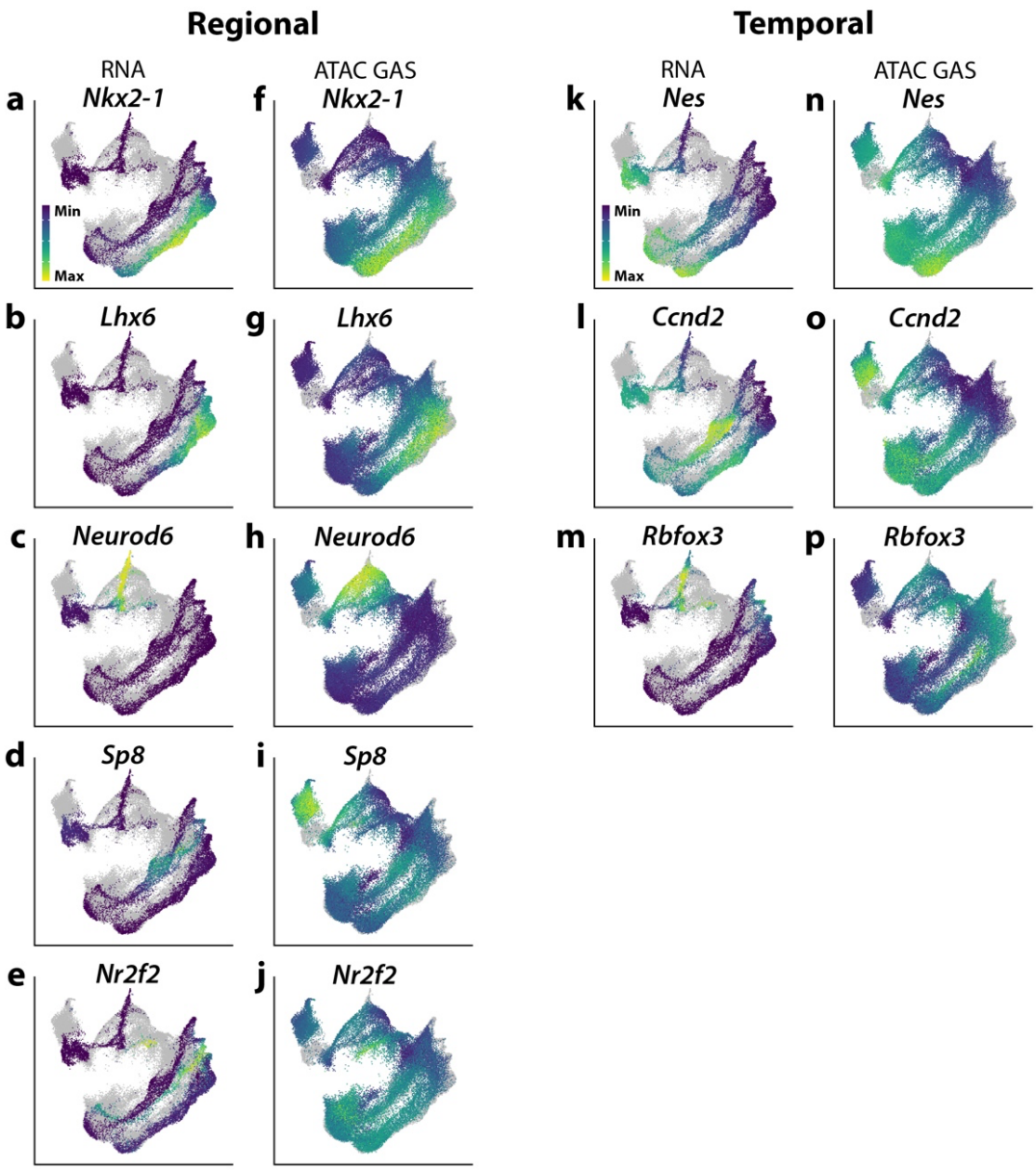

Extended Data Fig 5. Visualization of RNA counts and GAS following integration. UMAP visualization of transcript abundance from scRNA-Seq cells (left) and GAS from snATAC-seq nuclei (right) for genes enriched in specific brain regions (**a-j**) or in distinct neurogenic cell types (**k-p**).

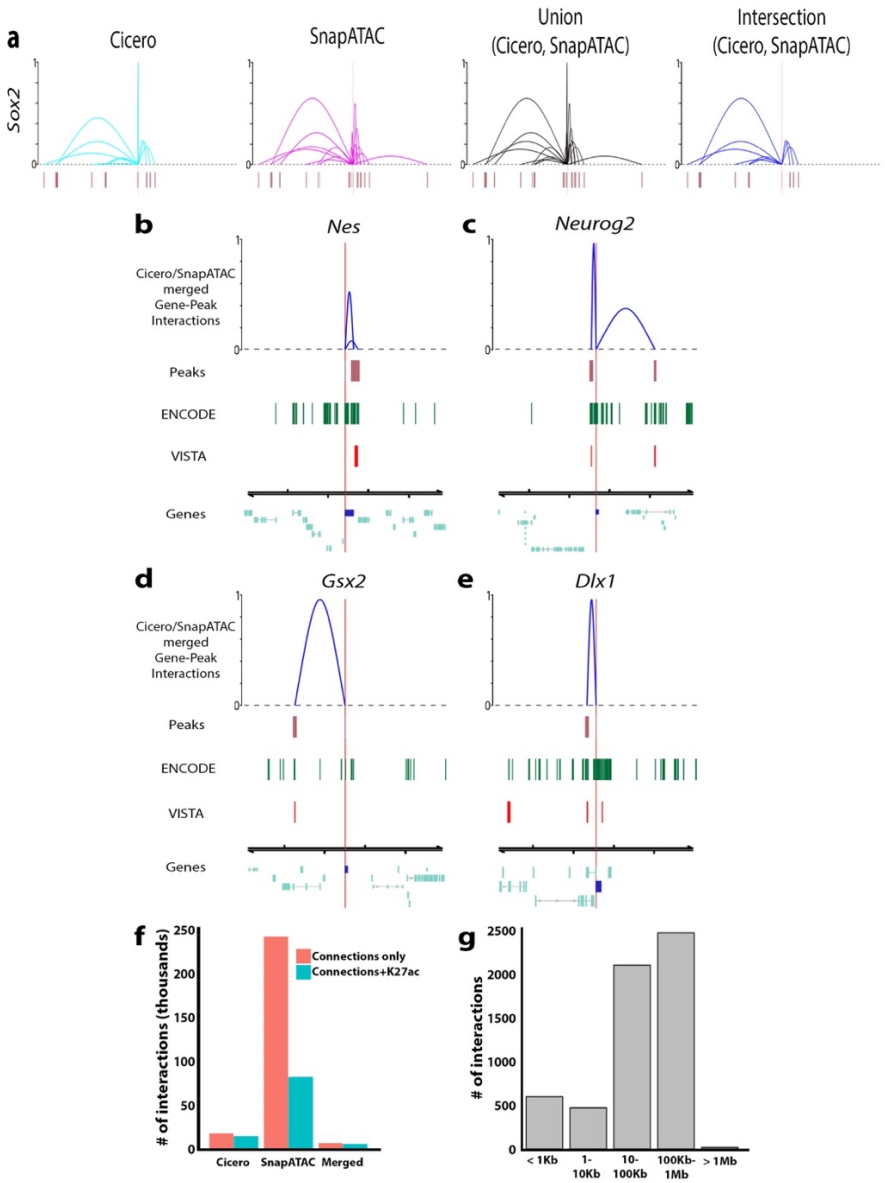

Extended Data Fig. 6. Characterization of enhancers in embryonic neurogenic tissue. a, Gene-enhancer interactions originating at the *Sox2* locus as defined by Cicero (cyan arcs), SnapATAC (magenta arcs), the combination of Cicero and SnapATAC (black arcs) and the intersection of Cicero and SnapATAC (dark blue arcs, representing high confidence enhancers). High confidence enhancers ("Intersection") were used for further analyses. Window is 0.5 Mb centered on TSS. Arc height represents interaction score. **b-e**, Visualization of intersection of Cicero and SnapATAC gene-peak interactions for *Nes* (**b**), *Neurog2* (**c**), *Gsx2* (**d**) and *Dlx1* (**e**). Window is 100 Kb, centered on the gene TSS. Peaks: displays co-accessible coordinates, Encode: displays H3K27ac signal from E12.5 forebrain from ENCODE ChIP-Seq data, VISTA: enhancers with positive activity in the forebrain and midbrain from the VISTA Enhancer Browser. **f**, Bar chart depicting the total number of gene-peak interactions detected by Cicero, SnapATAC and high-confidence interactions via the intersection of Cicero and SnapATAC ("merged" label). **G**, Bar chart of the number of gene-peak interactions binned by gene-peak distance for high-confidence gene-peak interactions.

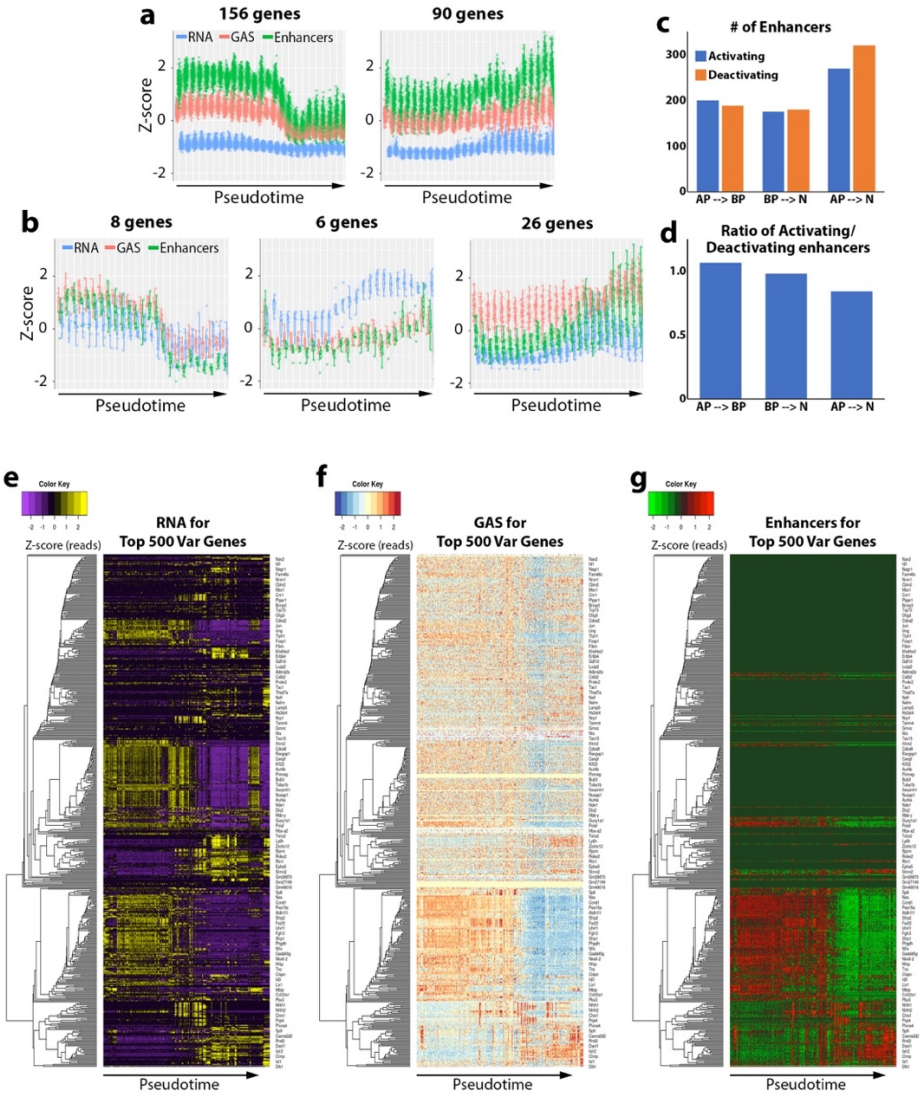

Extended Data Fig. 7. degPatterns analysis and heatmaps of RNA, GAS and enhancer counts for top 500 highly variable genes. a-b, Line graphs of genes within each cluster detected by degPatterns that contained > 5 genes per cluster using embryonic integrated snATAC-Seq/scRNA-Seq data. Y-axis is Z-score for RNA, GAS, or enhancers counts per gene. X-axis is binned pseudotime periods with origin corresponding to early development and higher pseudotime values corresponding to more differentiated cells. RNA, GAS, or enhancers for each gene in this cluster are plotted individually. **c**, Bar graph of change of enhancer usage for all detected H3K27ac+ presumptive enhancers associated with DEGs per state transition: AP to BP, BP to N and AP to N. All detectable H3K27ac+ presumptive enhancers defined as genomic intersection of 1) the genomic union of SnapATAC cREs and Cicero cREs with co-accessibility score >0.25) and 2) E12.5 ENCODE H3K27ac ChIP-Seq peaks. **d**, Bar graph of ratio of enhancer activation versus enhancer deactivation per state transition: AP to BP, BP to N and AP to N. **e-g**, Heatmaps of RNA (**e**), GAS (**f**) and enhancer (**g**) counts for top 500 highly variable genes from scRNA-Seq data and corresponding genes from snATAC-Seq GAS and enhancer matrices. Heatmap columns were ordered by hierarchical clustering with correlation distance and average linkage. Rows were ordered by pseudotime (assigned by Moncole3).

SUPPLEMENTARY TABLES

Supplementary Table 1: DA peaks per cluster
Supplementary Table 2: DA motifs per cluster
Supplementary Table 3: DA motifs filtered by DEGs
Supplementary Table 4: Embryonic enhancers
Supplementary Table 5: High-Confidence Embryonic Enhancers
Supplementary Table 6: High-Confidence Embryonic Enhancers Intersecting VISTA Enhancers
Supplementary Table 7: Oligos used for Capture-C